

Spin Models and Cluster Multipole Method: Application to Kagome Magnets

Juba Bouaziz,^{1,*} Takuya Nomoto,² and Ryotaro Arita^{1,3}

¹*Department of Physics, University of Tokyo, Tokyo 113-0033, Japan*

²*Department of Physics, Tokyo Metropolitan University, Hachioji, Tokyo 192-0397, Japan*

³*RIKEN Center for Emergent Matter Science (CEMS), Wako 351-0198, Japan*

(Dated: March 6, 2025)

We present a multi-scale computational approach that combines atomistic spin models with the cluster multipole (CMP) method. The CMP method enables a systematic and accurate generation of complex non-collinear magnetic structures using symmetry-adapted representations. The parameters of the spin model are derived from density functional theory using the magnetic force theorem, with the paramagnetic state as a reference. The energy landscape of CMP-generated structures is inspected at the model Hamiltonian level, and sets of low-energy magnetic structures are identified for each material candidate. The inclusion of relativistic antisymmetric and anisotropic pair interactions lifts partially the degeneracy among these most stable structures. To demonstrate the applicability and predictive capability of the method, we apply it to the non-collinear Mn_3X and collinear Fe_3X ($X = Ga, Ge, \text{ and } Sn$) kagome compounds. The computational efficiency of the method in identifying low-energy structures among multiple CMP configurations highlights its potential for high-throughput screening of complex magnets with unknown magnetic order.

I. INTRODUCTION

Magnetic crystals exhibit diverse forms of long-range order, including ferromagnetism [1], antiferromagnetism [2], and the recently identified altermagnetism, which is characterized by zero net magnetization and momentum-dependent spin polarization alternating in reciprocal space [3]. Beyond these collinear orders, magnetic moments can form non-collinear configurations, often arising from competing interatomic magnetic interactions [4–6]. The nature of these interactions is determined by factors such as chemical composition, dimensionality, and crystal symmetry.

Non-collinear magnetic orders manifest in various forms, ranging from commensurate triangular Néel states [7] and incommensurate magnetic helices [4, 8, 9] to more complex multiple- q states [10] and topological magnetic textures such as skyrmions and merons [11]. These intricate magnetic configurations strongly influence the electronic band structure, leading to topological features such as Weyl nodes [7, 12]. Signatures of these topological phenomena appear in magneto-transport properties, with a notable example being the large anomalous Hall effect observed in the non-collinear kagome antiferromagnet Mn_3Sn [7, 13, 14]. The absence of stray fields and the potential for high-speed processing make non-collinear antiferromagnets promising candidates for spintronics applications [15, 16].

Given the crucial role of magnetic order in determining a material’s functionality, several experimental techniques have been developed to probe it, with neutron scattering [17] and magneto-transport measurements [7, 11] being widely used. On the computational side, material-specific simulations using density func-

tional theory (DFT) have proven valuable in predicting and corroborating experimentally observed magnetic structures. High-throughput DFT calculations have been employed to investigate the magnetic ground state of collinear magnets [18] and non-collinear antiferromagnetic materials, using experimental magnetic structures as initial guesses [18]. A recently developed approach for non-collinear antiferromagnets involves evaluating within DFT the energy of constrained magnetic structures derived from the cluster multipole (CMP) method [19, 20]. The CMP approach uses magnetic and toroidal multipole expansions combined with a symmetry-adapted representation to generate an orthogonal basis set of candidate magnetic structures [21–23].

The DFT+CMP approach provides a unified framework for investigating both commensurate [19, 20] and incommensurate non-collinear magnetic orders [24]. However, its applicability is limited by high computational cost, convergence difficulties for certain non-collinear structures within constrained DFT, and the intrinsically low energy scale of magnetic interactions (meV) [19]. An alternative approach is to construct an atomistic spin model with parameters derived from DFT [25] and compare the energies of different CMP structures at the model Hamiltonian level. The key challenge then shifts to identifying a reliable spin Hamiltonian, which should: *(i)* reproduce the global energy landscape of arbitrary non-collinear configurations, *(ii)* respect the hierarchy of magnetic interactions by prioritizing the largest isotropic contributions (not limited to pair interactions), and *(iii)* incorporate non-isotropic interactions to distinguish between CMP structures with different chiralities.

Here, we present a multi-scale computational approach and systematically apply it to the complex kagome magnets Tm_3X family, including the non-collinear antiferromagnetic Mn_3X [12, 14, 26] and the collinear ferromagnetic Fe_3X which display large anomalous Hall effect and high curie temperatures [27, 28]. We identify

* jbouaziz@g.ecc.u-tokyo.ac.jp

the low-energy magnetic structures through DFT calculations which determine the atomistic spin model parameters, providing a faster and computationally efficient means to explore the full energy landscape of CMP structures. The parameters are derived from first principles using the magnetic force theorem [25, 29–33] in combination with the full-potential all-electron Korringa-Kohn-Rostoker (KKR) Green function method [34, 35]. To ensure that these parameters are independent of the reference state—an essential aspect for highly non-collinear magnetic systems—the mapping is performed from a paramagnetic reference state using the disordered local moment (DLM) approach [31, 36, 37]. The averaging over magnetic orientations to simulate the paramagnetic state is achieved via the coherent potential approximation [36, 38].

The paper is structured as follows. Sec. II outlines the employed methods, starting with the CMP approach, followed by the DLM method, and concluding with the alloy force theorem. The results are presented in Sec. III. First, we analyze the electronic structure of Tm_3X in the DLM state and examine the magnetic interactions in reciprocal space within the hexagonal Brillouin zone. Next, we investigate in detail the isotropic pair and biquadratic exchange parameters in real space. We then compute the energies of CMP structures using the generalized Heisenberg Hamiltonian, identify the low-energy configurations, and compare them with the results obtained from magnetic constraints. Finally, we incorporate relativistic interactions and demonstrate how they select specific structures among the lowest-energy ones. Sec. IV provides conclusions and an outlook on potential applications of the method. The appendices include detailed derivations of the exchange parameters in the ferromagnetic limit, accounting for relativistic effects, along with the complete set of CMP-generated structures.

II. METHODS

A. Cluster multipole (CMP) approach

We provide a concise overview of the CMP approach used to systematically generate the magnetic structures of the Tm_3X compounds. The details of this approach can be found in Refs. 21–23. This expansion constitutes a *discretization* of the standard multipolar expansion for a classical continuous vector potential in the Coulomb gauge [39] *focusing only on the spin magnetic moments*. The magnetic \mathcal{M}_{lm} and toroidal \mathcal{T}_{lm} multipoles for a collection of classical magnetic moments \mathbf{m}_i are introduced in a virtual atomic cluster which reflects the crystallographic point group of the actual crystal as [22]:

$$\mathcal{M}_{l\gamma} = \sum_{i=1}^{N_{\text{at}}} \mathbf{u}_{l\gamma i}^M \cdot \mathbf{m}_i, \quad \mathcal{T}_{l\gamma} = \sum_{i=1}^{N_{\text{at}}} \mathbf{u}_{l\gamma i}^T \cdot \mathbf{m}_i. \quad (1)$$

$$\begin{aligned} \mathbf{u}_{l\gamma i}^M &= \sqrt{\frac{4\pi}{2l+1}} \nabla \left[\mathcal{Y}_{l\gamma}^*(\hat{\mathbf{R}}_i) \right], \\ \mathbf{u}_{l\gamma i}^T &= \frac{1}{l+1} (\mathbf{u}_{l\gamma i}^M \times \mathbf{R}_i). \end{aligned} \quad (2)$$

\mathbf{R}_i indicates the position of the moment \mathbf{m}_i . N_{at} designates the numbers of atoms in the cluster and l is the angular momentum quantum number. For a physically meaningful expansion, the multipole basis functions $\mathbf{u}_{l\gamma i}^M$ and $\mathbf{u}_{l\gamma i}^T$ are given in terms of the spherical harmonics $\mathcal{Y}_{l\gamma}(\hat{\mathbf{R}}_i)$ which are symmetrized according to irreducible representations of the crystallographic point group:

$$\mathcal{Y}_{l\gamma}(\hat{\mathbf{R}}_i) = \sum_m c_m^\gamma Y_{lm}(\hat{\mathbf{R}}_i) \quad . \quad (3)$$

m is the magnetic quantum number and $Y_{lm}(\hat{\mathbf{R}}_i)$ are the complex spherical harmonics. The c_m^γ coefficients are defined and tabulated in Ref. 40 with $1 \leq \gamma \leq 2l+1$.

Using Eqs. (1) and (2), the atomic positions \mathbf{R}_i relative to the origin of the atomic cluster are sufficient to unambiguously define $\mathcal{M}_{l\gamma}$ and $\mathcal{T}_{l\gamma}$, with N_{at} fixed to the number of symmetry operations of the crystallographic point group. The next step is to obtain the multipoles for the *real crystal*. Focusing on commensurate magnetic structures ($\mathbf{q} = 0$), this mapping procedure involves identifying cluster atoms transformed by point-group symmetry operations with their corresponding real crystal atoms transformed by space-group symmetry operations [22]. The mapping is not unique; for example, convenient choices are provided for the C_{4h} point group in crystals with space groups $P4/m$ and $P4_2/m$ in Ref. 22. The multipole basis functions $\mathbf{u}_{l\gamma i}^M$ and $\mathbf{u}_{l\gamma i}^T$ for the real crystal is a complete basis defined in terms of spherical harmonics (Eq. (2)), they are orthogonalized using Gram-Schmidt orthonormalization procedure [19, 22].

The CMP structures generated are based on the symmetry of the crystal and do not contain information on its the magnetic energy landscape. The *central assumption* within this approach is that *the magnetic ground-state configuration is present among the CMP structures*, or a more elaborate scheme involving *combining uniformly weighted CMPs of the same order and irreducible representation* [19]. This assumption was corroborated by comparing the experimental magnetic space groups from MAGNDATA [41] for 131 materials, with 90.16% of them agreeing with the CMP structures. In practice, this means that the ground state configuration for the moments \mathbf{m}_i is given by the basis functions $\mathbf{u}_{l\gamma i}^M$ or $\mathbf{u}_{l\gamma i}^T$, and the magnetic order is described by the CMPs. The CMP structures for the Tm_3X compounds studied here are generated numerically following the procedure outlined above [22]. For simplicity, these structures are labeled with an integer index N_{mltp} in Sec. III E. A detailed listing of each CMP structure, including their order (l) and types (magnetic or toroidal), is provided in Appendix C.

B. Disordered Local Moment

The magnetic order and electronic properties of the Tm_3X are investigated in the paramagnetic state, which is modeled using the disordered local moment (DLM) theory [36] within spin density functional theory. The later accounts for the magnetic transverse fluctuations at finite temperature. The DLM approach is suitable for systems with strong local magnetic moment such as the Fe/Mn compounds under investigation [36, 42]. It relies on an adiabatic separation which assumes that the dynamics of the local magnetic moments \mathbf{m}_i is slower than the electronic degrees of freedom, thus the magnetic order at finite temperature within DFT can be modeled using various magnetic configurations of the local moments \mathbf{m}_i [36]. The averages over the magnetic configurations are conveniently performed using the CPA in as implemented with the KKR Green function approach [43].

In the non-relativistic limit and considering the rotational symmetry of the paramagnetic state, the DLM calculations can be mapped on a binary pseudo alloy with equal ‘‘up’’ and ‘‘down’’ concentrations [36, 44, 45]. The CPA approach is based on the construction of an effective medium [38]. For a binary alloy which consists of two species A_xB_{1-x} (x being the concentration of the A specie), the site diagonal part of the KKR structural Green function (see Eq. (A4)) for the effective medium according to the CPA condition reads [45]:

$$\mathbf{G}_{ii}^c = x \bar{\mathbf{G}}_{ii}^A + (1-x) \bar{\mathbf{G}}_{ii}^B. \quad (4)$$

\mathbf{G}_{ii}^c is a matrix in spin and orbital space (σ, L) . The local Green function of the specie Q is obtained by embedding the scattering matrix of the element Q (\mathbf{t}_i^Q) into the effective medium as follows:

$$\bar{\mathbf{G}}_{ii}^Q = \mathbf{G}_{ii}^c [1 - (\mathbf{t}_i^Q - \mathbf{t}_i^c) \mathbf{G}_{ii}^c]^{-1}. \quad (5)$$

\mathbf{t}_i^c is the scattering matrix of the effective medium. The central quantity of interest are the isotropic exchange interactions (pair or biquadratic) in the DLM state (see Sec. II C). These are computed via the site off-diagonal Green functions $\mathbf{G}_{ij}^{QQ'}$ which is given in the CPA framework by the conditionally averaged Green functions [25, 31, 46]:

$$\bar{\mathbf{G}}_{ij}^{QQ'} = [1 - \mathbf{G}_{ii}^c (\mathbf{t}_i^Q - \mathbf{t}_i^c)]^{-1} \mathbf{G}_{ij}^c [1 - (\mathbf{t}_j^{Q'} - \mathbf{t}_j^c) \mathbf{G}_{jj}^c]^{-1}. \quad (6)$$

This renormalization of the effective medium’s structural non-local Green function \mathbf{G}_{ij}^c is adequate for a good description of the fully paramagnetic DLM state and strong scattering limit [25, 31].

C. Alloy force theorem

In order to compute the magnetic interactions starting from paramagnetic state using the pseudo alloy with equal ‘‘up’’ and ‘‘down’’ concentrations [45], i.e. the DLM

state, we consider the alloy version of the magnetic force theorem [25, 31, 47]. Taking a binary alloy A_xB_{1-x} (x being the concentration of the A specie) with infinitesimal rotations of the local moments, the vertex corrections are cancelled to first order [47]. Therefore, the magnetic exchange interactions can be extracted similarly to ferromagnetically ordered systems [25]. The detailed derivation of the pair [30, 32, 33] and biquadratic/higher order interactions [48–50] for the ferromagnetic state are provided in Appendix A. For the alloy, the variation of the grand canonical potential $\delta\Omega$ is obtained from the Lloyds formula [51, 52]:

$$\delta\Omega = \frac{1}{\pi} \text{Im} \text{Tr}_{i\sigma Q} \int_{-\infty}^{E_F} dE \ln(1 - \bar{\mathbf{G}}\delta\mathbf{V}) \quad , \quad (7)$$

where the trace is taken over spin (σ), sites (i) and atomic species (Q). The system’s averaged Green functions $\bar{\mathbf{G}}$ is obtained using the CPA approach (see Sec. II B) and $\delta\mathbf{V}$ is the variation of potential due to an infinitesimal rotation of the magnetic moments. The analytical expression of the pair isotropic exchange is obtained from the second order expansion (see Appendix A and Eq. (B3)) of $\delta\Omega$ [25, 31]:

$$J_{ij}^{QQ'} = \frac{1}{2\pi} \text{Im} \text{Tr}_{\sigma,L} \int_{-\infty}^{E_F} dE \bar{\mathbf{G}}_{ij}^{QQ'}(E) \mathbf{B}_j^{x,Q'}(E) \bar{\mathbf{G}}_{ji}^{Q'Q}(E) \mathbf{B}_i^{x,Q}(E) \quad . \quad (8)$$

$\bar{\mathbf{G}}_{ij}^{QQ'}(E)$ is the alloy structural Green function obtained from Eq. (6). $\mathbf{B}_i^{x,Q}(E)$ is the exchange splitting at site i , of the specie Q as defined in Eq. A6. The mapping is done onto a pair Heisenberg Hamiltonian for the alloy (\mathcal{H}_A):

$$\mathcal{H}_A = - \sum_{i \neq j} \sum_{QQ'} J_{ij}^{QQ'} (\mathbf{e}_i^Q \cdot \mathbf{e}_j^{Q'}) \quad , \quad (9)$$

where $\{Q, Q'\} = \{A, B\}$ for the binary alloy. In the particular case of the DLM state, the following symmetry relations apply $J_{ij}^{\uparrow\uparrow} = J_{ij}^{\downarrow\downarrow}$ and $J_{ij}^{\uparrow\downarrow} = -J_{ij}^{\downarrow\uparrow}$. Therefore, $\{Q, Q'\} = \{\uparrow, \uparrow\}$ is sufficient to extract the magnetic interactions in the DLM state. Eq. (8) is then simplified further by introducing $\bar{\mathbf{G}}_{ij}(E) = \bar{\mathbf{G}}_{ij}^{\uparrow\uparrow}(E)$:

$$J_{ij} = \frac{1}{2\pi} \text{Im} \text{Tr}_{\sigma,L} \int_{-\infty}^{E_F} dE \bar{\mathbf{G}}_{ij} \mathbf{B}_j^{x,\uparrow} \bar{\mathbf{G}}_{ji} \mathbf{B}_i^{x,\uparrow} \quad . \quad (10)$$

The explicit energy dependencies are dropped for a more compact expression. The isotropic biquadratic interactions in the DLM state are extracted using the fourth order expansion (see Appendix A and Eq. (B7)) of $\delta\Omega$ [49]:

$$B_{ij} = \frac{1}{2\pi} \text{Im} \text{Tr}_{\sigma,L} \int_{-\infty}^{E_F} dE [\bar{\mathbf{G}}_{ij} \mathbf{B}_j^{x,\uparrow} \bar{\mathbf{G}}_{ji} \mathbf{B}_i^{x,\uparrow}] \times [\bar{\mathbf{G}}_{ij} \mathbf{B}_j^{x,\uparrow} \bar{\mathbf{G}}_{ji} \mathbf{B}_i^{x,\uparrow}] \quad . \quad (11)$$

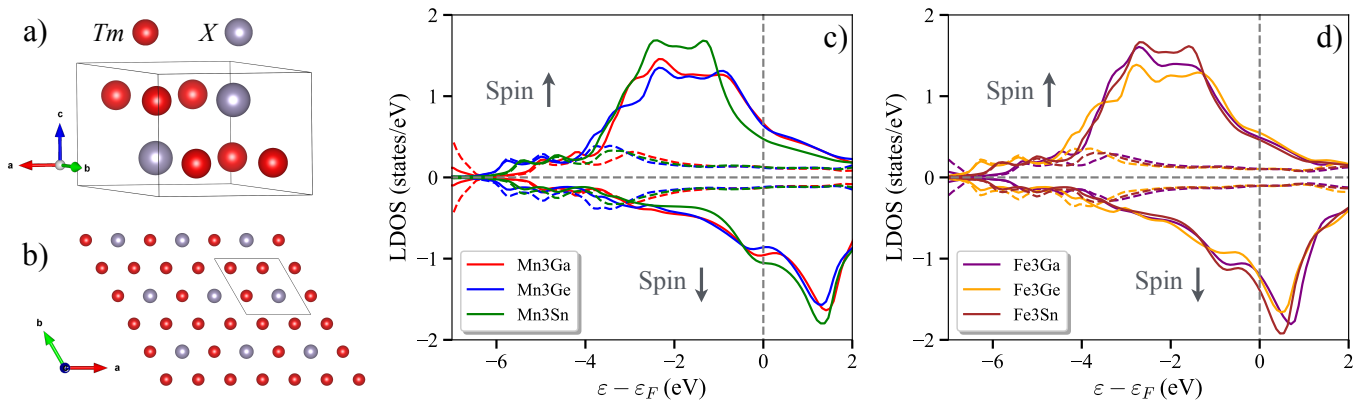


FIG. 1. a) Side view of the Tm_3X ($Tm = Mn, Fe$; $X = Ga, Ge, Sn$) unit cell, showing two layers at $z = c/4$ and $z = 3c/4$. b) Top view of the ab plane at $z = c/4$, where the Tm atoms form a kagome lattice and the X atoms form a hexagonal lattice. c-d) Spin-resolved paramagnetic local density of states (LDOS) per atom. Solid (dashed) lines represent Tm (X) elements. The nearly filled up-spin channel and partially filled down-spin channel result in a high LDOS at the Fermi energy, indicating their metallic nature. c) Mn_3X and d) Fe_3X ($X = Ga, Ge, Sn$).

The biquadratic interactions obtained from Eq. (11) for elemental itinerant magnets such as bcc Fe and fcc/hcp Co are found to be in very good agreement with the ones obtained from the DLM based spin cluster expansion technique [53, 54]. The Heisenberg model Hamiltonian including isotropic non-relativistic pair and biquadratic interactions reads:

$$\mathcal{H} = - \sum_{ij} J_{ij} (\mathbf{e}_i \cdot \mathbf{e}_j) - \sum_{ij} B_{ij} (\mathbf{e}_i \cdot \mathbf{e}_j)^2 \quad (12)$$

\mathbf{e}_i being a the unit vector for the classical magnetic moments \mathbf{m}_i introduced in Sec. II A. The inclusion of relativistic spin-orbit interactions introduces more complex terms to the Hamiltonian including anti-symmetric terms and symmetric anisotropic terms [33, 55]. The anti-symmetric Dzyaloshinskii–Moriya interaction [56, 57] in the Mn_3X compounds is addressed in Sec. III G.

III. RESULTS AND DISCUSSION

A. Crystal and electronic structure

The first-principles calculations were performed using the all-electron full-potential KKR Green function method [58] within the scalar relativistic approximation, employing $l_{\max} = 3$ for the orbital expansion of the Green function. The self-consistent calculations are performed using a k-mesh of $25 \times 25 \times 25$, an energy contour containing 58 energy points and an electronic smearing temperature of 500 K. The paramagnetic electronic structure is obtained using the charge self-consistent DLM approach [31]. The magnetic exchange interactions are extracted using the alloy force theorem (see Sec. II C) using a denser k-mesh $30 \times 30 \times 30$ and an electronic temperature of 300 K.

We focus on the Tm_3X ($Tm = Mn, Fe$; $X = Ga, Ge, Sn$) compounds in their DO_{19} structure, which belongs to the hexagonal space group $P63/mmc$. The unit cell, shown in Fig. 1a, contains eight atoms (six Tm and two X atoms). The Tm atoms occupy two distinct layers ($z = c/4$ and $z = 3c/4$), each layer forming a two-dimensional kagome lattice (see Fig. 1b). The hexagonal lattice constants (a, c) are taken from experiment and given in Table I.

The paramagnetic local density of states (LDOS) for one representative Tm and X atom of Tm_3X is shown in Figs. 1c-d. It consists of the imaginary part of the local Green function for the \uparrow -component of the pseudo-alloy. The electronic structure is broadened due to the thermal magnetic fluctuation [59]. The local magnetic moment (spin-splitting) is present on the Tm sites while the X atoms are non-magnetic in contrast to the ferromagnetic state where the spd -orbitals of X acquire an induced spin polarization. The high density of states at the Fermi energy indicates that systems are metallic and the Tm magnetic moments likely interact via an indirect Ruderman–Kittel–Kasuya–Yosida (RKKY) exchange mechanism [60]. Note that for the Mn_3Ga and Fe_3Ga compounds, the Ga $3d$ -states are visible at around $\varepsilon \simeq -7$ eV away from the Fermi energy. The localization of the magnetic moment on the Tm sites makes a convenient state to map onto a Heisenberg model [36]. The comparison between the Mn and Fe LDOS shows that the additional electron in the Fe $3d$ spin down channel systematically lead to a reduction the spin moment of Fe_3X with respect to Mn_3X as shown in Table I, which is also in agreement with Hund’s rules independently of the non-magnetic X -elements. For both Mn_3X and Fe_3X , the largest magnetic moments are obtained for $X = Sn$, intermediate moments for $X = Ga$, and the smallest for $X = Ge$ (see Table I). The calculated magnetic moments on the Tm atoms are compared with experimental val-

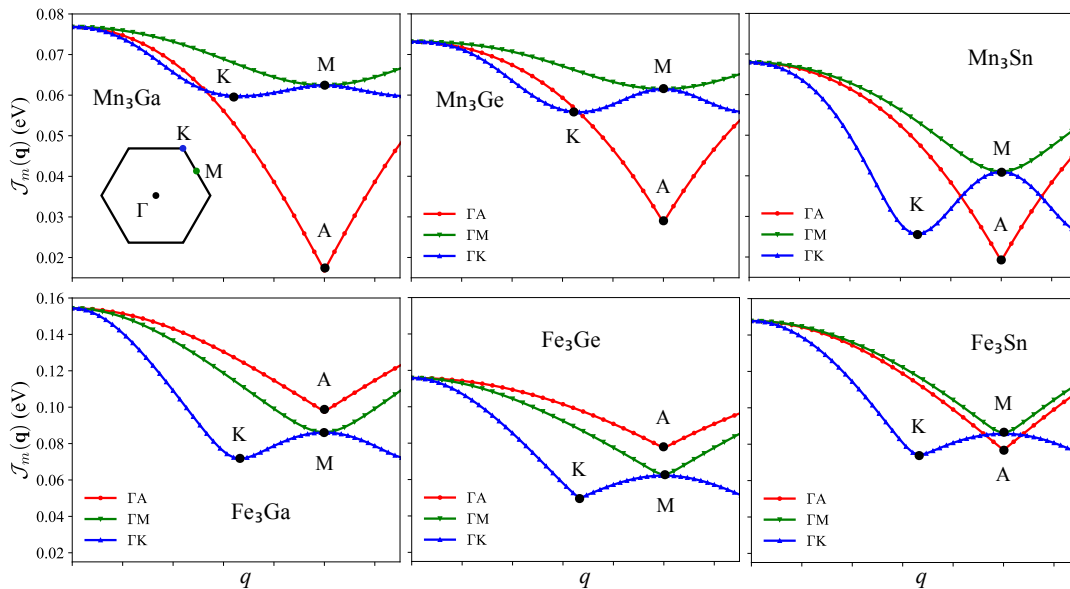


FIG. 2. The maximal eigenvalue, $\mathcal{J}_m(\mathbf{q})$, is shown for all Tm_3X compounds. Three high-symmetry lines in the hexagonal Brillouin zone are shown: ΓA , ΓM , and ΓK . The inset in the first panel illustrates the two-dimensional Brillouin zone, marking the (M, K) points, while the A point lies along the c -direction. The x -axis has been rescaled to better display the dispersion and symmetry of $\mathcal{J}_m(\mathbf{q})$.

Tm_3X	a (Å)	c (Å)	$M^{\text{exp}}(\mu_B)$	$M_{\text{DLM}}(\mu_B)$
Mn ₃ Ga[26]	5.360	4.325	2.40	2.76
Mn ₃ Ge[61]	5.360	4.320	2.50[62]	2.65
Mn ₃ Sn[63]	5.665	4.531	3.17	3.22
Fe ₃ Ga[64]	5.200	4.360	2.03[65]	2.24
Fe ₃ Ge[66]	5.178	4.226	2.20[28]	2.04
Fe ₃ Sn[67]	5.457	4.362	2.37[27]	2.27

TABLE I. Experimental lattice constant parameters for the studied Tm_3X compounds. The magnetic moments obtained from experiment (M^{exp}) and the spin moments from the present calculations (M_{DLM}) are shown in the last two rows.

ues, which were measured at different temperatures and include error bars. Overall, the results show reasonable agreement: the moments of Mn₃X and Fe₃Ga are slightly overestimated, while those of Fe₃Ge and Fe₃Sn are underestimated.

B. Magnetic interactions in reciprocal space

The Tm_3X family has different competing magnetic interactions at play which give it its rich and complex magnetic phase diagram. Here, we focus on the isotropic magnetic interactions J_{ij} , computed from the DLM state which determine the transition temperature (T_p) from a magnetically ordered state to a paramagnetic one, and the possible emergence of incommensurate magnetic order below T_p due to frustrated exchange interactions [8, 68]. Considering the translation symmetry of Tm_3X containing six sites per unit cell, it is convenient

to split the site indices $\{i, j\}$ introduced in Eq. (12) into $i = \{m, k\}$, where m indicates the atomic index in the unit cell and k is the cell index with the position \mathbf{R}_m^k . The Fourier transform of the isotropic pair interactions reads:

$$\mathcal{J}_{mn}(\mathbf{q}) = \sum_{k=1}^{N_c} e^{i\mathbf{q}\cdot(\mathbf{R}_n^k - \mathbf{R}_m^0)} J_{mn}^{0k} \quad (13)$$

N_c is the number of unit cells, and $\mathcal{J}(\mathbf{q})$ is a 6×6 matrix. The Fourier transforms are computed with a real-space cutoff $R_{\text{cut}} = 2a$ (where a is the in-plane lattice constant), a distance at which all J_{ij} for Tm_3X vanish as shown in Fig. 4. We now inspect the dispersion along three high-symmetry directions within the hexagonal Brillouin zone of the highest eigen value of $\mathcal{J}(\mathbf{q})$, $\mathcal{J}_m(\mathbf{q})$. The results are shown in Fig. 2, the wave vector \mathbf{q}_m that maximizes $\mathcal{J}_m(\mathbf{q})$ determines the lowest-energy magnetic modulation [8, 9, 69]. For all Tm_3X compounds, $\mathcal{J}_m(\mathbf{q})$ reaches its maximum at $\mathbf{q}_m = 0$, indicating that the magnetic structures are commensurate between crystallographic cells. For Mn₃X compounds, these results are in good agreement with Ref. 69, where it was found that magneto-elastic effects do not lead to the formation of incommensurate magnetic order. The magnetic structure within each cell will be analyzed in details in Sec. III E using the CMP-generated magnetic structures. We note that, for Mn₃Sn in the low-temperature regime, an incommensurate helical magnetic order emerges along the c -direction [60, 63, 70, 71], characterized by a wave vector $q_z = 0.09(2\pi/c)$. This incommensurate ordering is reproduced when the exchange parameters are derived from

Tm_3X	T_p^{th} (K)	T_p^{exp} (K)
Mn_3Ga	594.2	470 [26]
Mn_3Ge	566.1	380 [62]
Mn_3Sn	525.8	420 [72]
Fe_3Ga	1194.1	720 [65]
Fe_3Ge	896.1	640 [28]
Fe_3Sn	1142.8	725 [27]

TABLE II. Comparison between the theoretical and experimental transition temperatures of Tm_3X in Kelvin (K). The theoretical values T_p are obtained using the mean-field approximation (using Eq. 14), while the experimental values T_p^{exp} are taken from previous measurements.

the ferromagnetic reference state and including Hubbard (U, J) to the DFT exchange-correlation potential [60].

At the mean-field level, the key quantity for determining the transition temperature is $\mathcal{J}_m(\mathbf{q}_m)$, and T_p reads [31]:

$$T_p = \frac{2}{3k_b} \mathcal{J}_m(0) \quad , \quad (14)$$

where k_b is the Boltzmann constant. The obtained T_p values for all Tm_3X compounds are provided in Table II, which also includes the corresponding experimental values. The calculated T_p values are systematically higher than the experimental ones, as expected from a mean-field approximation [69]. The experimental trends are well reproduced for the Mn_3Ga , Mn_3Sn , and Fe_3X compounds, with the exception of the Mn_3Ge system, where the computed T_p value exceeds that of Mn_3Sn .

C. Magnetic interactions in real space: pair exchange

We now examine the real-space dependence of the isotropic pair magnetic interactions J_{ij} . The Tm_3X compounds contain six atoms per unit cell, so the full exchange matrix has a size of 6×6 and a cell dependence (J_{mn}^{kl} introduced in Sec. III B). The components of this matrix are determined using Eq. (10). The different sites within each plane ($z = c/4$ and $z = 3c/4$) are related by C_3 symmetry, while the atoms from one kagome layer are related to their partners in the other layer via inversion symmetry, e.g. atom A in Fig. 3 transforms into a . The analysis of couplings between the different sublattices in Fig. 3 allows the reduction of the full exchange matrix to a group of four representative interactions.

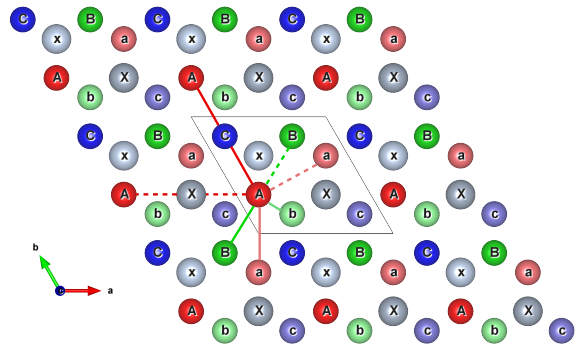


FIG. 3. The top view of the unit cell shows the Tm sites at $c = z/4$, denoted by capital letters A, B, and C, while the non-magnetic site is labeled X. The sites at $c = 3z/4$ are represented by lowercase letters a, b, c, and x. The primitive cell is outlined by the black rhombus. The bonds indicate the four representative interactions analyzed. Inequivalent interactions at equal distances are depicted using solid and dashed lines.

The magnetic interactions for all the Tm_3X compounds are shown in Fig. 4. Each panel contains four groups: AA, AB, Aa, and Ab. Within our spin Hamiltonian convention, positive interactions indicate ferromagnetic coupling (FM), while negative interactions signify antiferromagnetic coupling (AFM). The interactions exhibit oscillatory negative and positive values up to a range of $1.5a$ (a being the in-plane lattice constant), which do not necessarily follow an RKKY exchange decay. This behavior aligns with previous theoretical and experimental findings for Mn_3Sn in Ref.[60], where it was suggested that the discrepancy may arise either from the non-sphericity of the Fermi surface [71] or from multi-band contributions [73]. A common feature observed across all Tm_3X compounds is the inequivalence of the first nearest-neighbor (NN) interactions for AB coupling. This arises because the connecting bond either includes an X or Mn atom on the top left (Fig. 3), leading to significantly different AB interactions, which may even be opposite in nature, as observed in Mn_3Ge and Mn_3Sn [74]. Similarly, inequivalence is evident in the interlayer couplings Aa, where the connecting bond involves either two X atoms or two Tm atoms (Fig. 3). Lastly, the AA coupling within the same plane is non-negligible and exhibits a substantial splitting at similar distances for Mn_3Ge , Mn_3Sn , and all Fe_3X compounds. This difference arises from whether the connecting bond passes through a Tm atom or an X atom (Fig. 3).

The Mn compounds shown in the first row of Fig. 4 exhibit interlayer nearest-neighbor (NN) Ab coupling that favors an antiferromagnetic (AFM) order. Among them, Mn_3Ge has the largest values, while Mn_3Sn exhibits the smallest. The NN interlayer Aa coupling is systematically ferromagnetic (FM), whereas the NN interaction for AA coupling is AFM. These AA couplings, which represent interactions between atom A and another atom A in the adjacent unit cell along the c -direction, are not

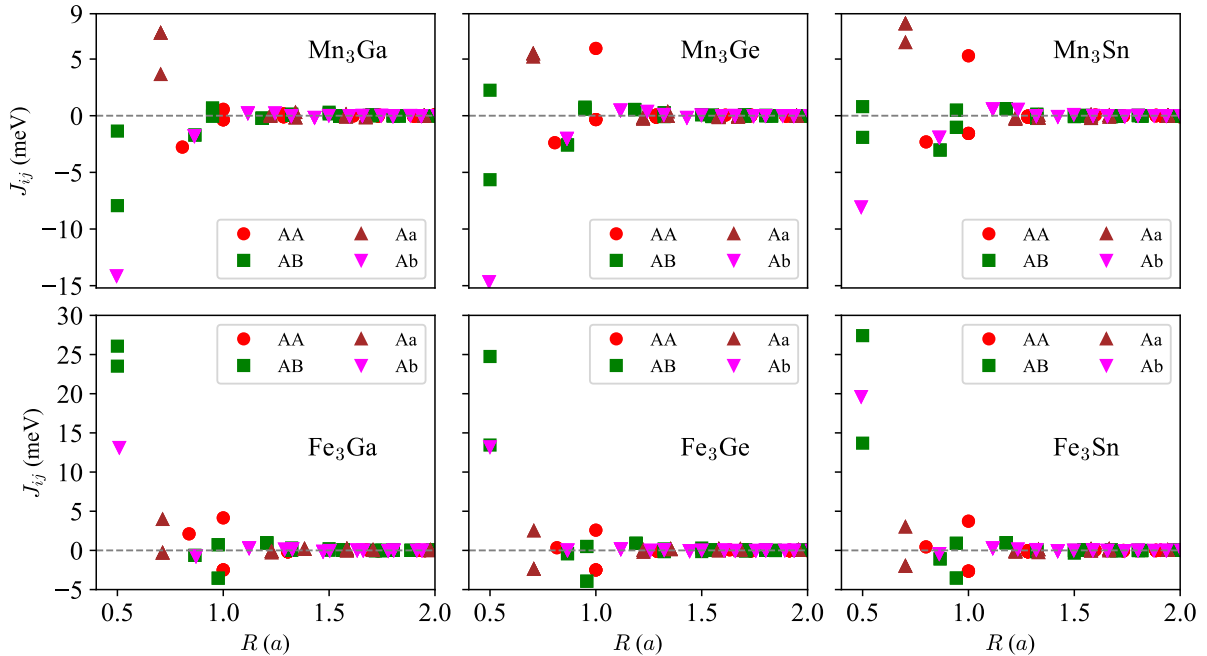


FIG. 4. Isotropic pair interactions J_{ij} as a function of the interatomic distance R (given in units of the in plane lattice constant a) for the representative sublattice couplings: AA, Aa, AB, and Ab, indicated in different colors. Each panel corresponds to one of the Tm_3X compounds ($Tm = Mn, Fe; X = Ga, Ge, Sn$). The in plane exchange interactions in Mn_3X favors antiferromagnetism, while in Fe_3X , it tends to be ferromagnetic.

displayed in Fig. 3. The Fe_3X compounds under consideration exhibit strong FM interactions for both AB and Ab couplings. AFM interactions are observed for the AA coupling between next-nearest neighbors (in-plane), for third neighbors in the AB coupling, and for NN in the Aa coupling. Despite the presence of these AFM interactions, the strong NN FM interactions for Ab and AB couplings dominate in magnitude. Overall, the comparison between Mn_3X and Fe_3X compounds reveals that the former tends toward AFM orders, while the latter favors FM orders.

D. Magnetic interactions in real space: biquadratic exchange

Having analyzed the pair isotropic interactions, we now turn to the biquadratic isotropic interactions, B_{ij} , which represent the next largest isotropic contributions. Within our spin Hamiltonian convention (see Eq. (12)), a positive B_{ij} coefficient favors collinear alignment of magnetic moments, whereas a negative B_{ij} promotes perpendicular alignment. The biquadratic interactions share the same symmetry properties as the pair isotropic interactions with respect to the real-space indices (i, j) . Consequently, similar to the J_{ij} parameters, the B_{ij} interactions will be discussed in terms of the representative groups AA, AB, Aa, and Ab, as depicted in Figure 5. The range of the B_{ij} coefficients is significantly shorter

than that of the J_{ij} . Beyond the first nearest neighbor (NN) for each group, these interactions become negligibly small. This behavior is consistent with the analytical expression for B_{ij} (Eq. (11)), which involves a fourth-order product of non-local Green's functions that decay with increasing interatomic distance. In contrast, the J_{ij} interactions depend on a second-order product of Green's functions (Eq. (8)), resulting in a slower decay. A similarly rapid decay of the B_{ij} parameters has been calculated for bcc Fe iron [49, 54] and Ru-based Heusler alloys [75].

For all Mn compounds, the B_{ij} coefficients favor a perpendicular alignment. In the Ab group, the NN B_{ij} values are $0.16J_{ij}$ for Mn_3Ga and Mn_3Ge , and $0.35J_{ij}$ for Mn_3Sn . For the AB group, the B_{ij} coefficients at the same distance exhibit a splitting analogous to the J_{ij} , arising from the inequivalence of the bonds, as previously discussed (see Fig. 3). The trend remains consistent: weaker J_{ij} correspond to weaker B_{ij} . On one hand, the largest AB biquadratic interaction for Mn_3Ga is $0.15J_{ij}$, while for Mn_3Ge , it is $0.34J_{ij}$. On the other hand, B_{ij} for Mn_3Sn exceeds the corresponding J_{ij} , reaching $1.47J_{ij}$. The interlayer Aa biquadratic interactions are negative and relatively weak compared to the Ab and AB interactions. For the Fe compounds, the largest B_{ij} coefficients are again associated with the Ab coupling, favoring a collinear alignment. In Fe_3Ga , the AB couplings promote a perpendicular alignment, whereas they favor a collinear configuration in Fe_3Ge and Fe_3Sn . Addition-

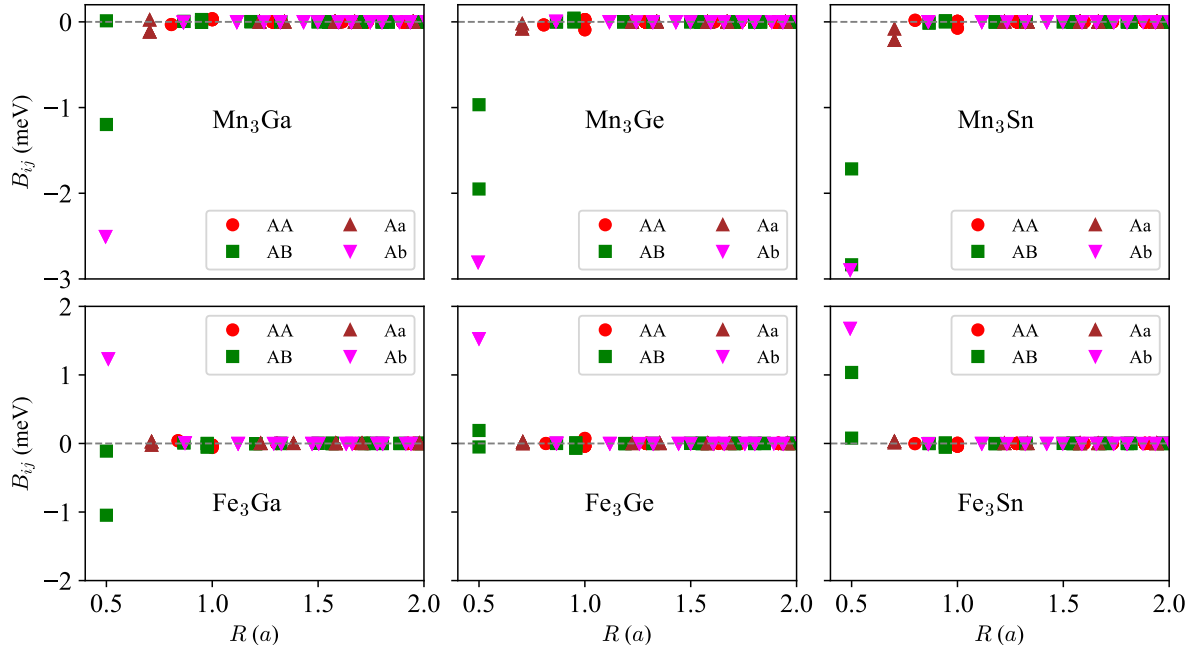


FIG. 5. Isotropic biquadratic interactions B_{ij} as a function of the interatomic distance R (given in units of the in plane lattice constant a) for the representative sublattice couplings: AA, Aa, AB, and Ab, indicated in different colors. Each panel corresponds to one of the Tm_3X compounds ($Tm = \text{Mn, Fe}$; $X = \text{Ga, Ge, Sn}$). The B_{ij} interactions have a shorter spatial range compared to the J_{ij} interactions and promote a perpendicular alignment of the magnetic moments in the Mn_3X compounds.

ally, the B_{ij} coefficients for the Aa couplings are negligibly small. Overall, the largest B_{ij} values are obtained for nearest AB and Ab couplings for all the Tm_3X compounds.

The significance of higher-order terms in Mn_3X compounds has already been highlighted in Refs. 69 and 76, which used a Weiss field-based DLM approach [36] and total energy fits to extract effective spin model parameters, respectively. These studies also identified isotropic multi-site interactions, such as three-site interactions between Mn triangles. Such interactions, however, are not included in the present study and will be addressed in future work.

E. Cluster multipole energies

Considering the DLM reference state magnetic interactions, all the Tm_3X systems under investigation exhibit a commensurate magnetic order, i.e., Fourier transforms peak at $\mathbf{q}_m = 0$, as shown in Sec. III B. Therefore, the magnetic Hamiltonian given in Eq. (12) will be restricted to these commensurate structures and recast as in Eq. (13) using sublattice (m, n) and cell (k, l) indices [74]:

$$\mathcal{H} = - \sum_{kl, mn} J_{mn}^{kl} (\mathbf{e}_m^k \cdot \mathbf{e}_n^l) - \sum_{kl, mn} B_{mn}^{kl} (\mathbf{e}_m^k \cdot \mathbf{e}_n^l)^2, \quad (15)$$

and the Hamiltonian per unit cell is then given by:

$$\mathcal{H}_c = - \sum_{mn} \mathcal{J}_{mn} (\mathbf{e}_m \cdot \mathbf{e}_n) - \sum_{mn} \mathcal{B}_{mn} (\mathbf{e}_m \cdot \mathbf{e}_n)^2. \quad (16)$$

The sublattice interactions are defined as $\mathcal{J}_{mn} = \sum_l J_{mn}^{0l}$, and \mathbf{e}_n represents the unit vector of cell 0 for sublattice n . The summation m, n in Eq. (16) runs over all sublattices {A, B, C, a, b, c} in the Tm_3X unit cell. The values of the sublattice pair (\mathcal{J}_{mn}) and biquadratic (\mathcal{B}_{mn}) interactions are provided in Table III.

We now systematically compare the magnetic energy per unit cell using Eq. (16), considering multiple commensurate collinear and non-collinear structures generated using the CMP method (see Sec. II A). The CMP generates a total of 14 structures for which the moments \mathbf{m}_i have fixed magnitude, all of which are presented in Appendix C. Fig. 6 a-d show the energies as a function of the Nmltp (multipole index). Several CMP solutions are degenerate, as only isotropic interactions are included. At this point, the aim is to determine, out of all the possible CMP structures, lowest energy sets by considering the largest isotropic magnetic interactions (pair and biquadratic).

Fig. 6a shows the energy landscape including \mathcal{J}_{mn} terms. These split into two separate groups: one for Mn_3X and one for Fe_3X . The first group, Mn_3X , has four non-collinear degenerate lowest energy solutions, which are depicted in Fig. 6e (Nmltp=4,5,9,10). These results are in agreement with previous findings from the

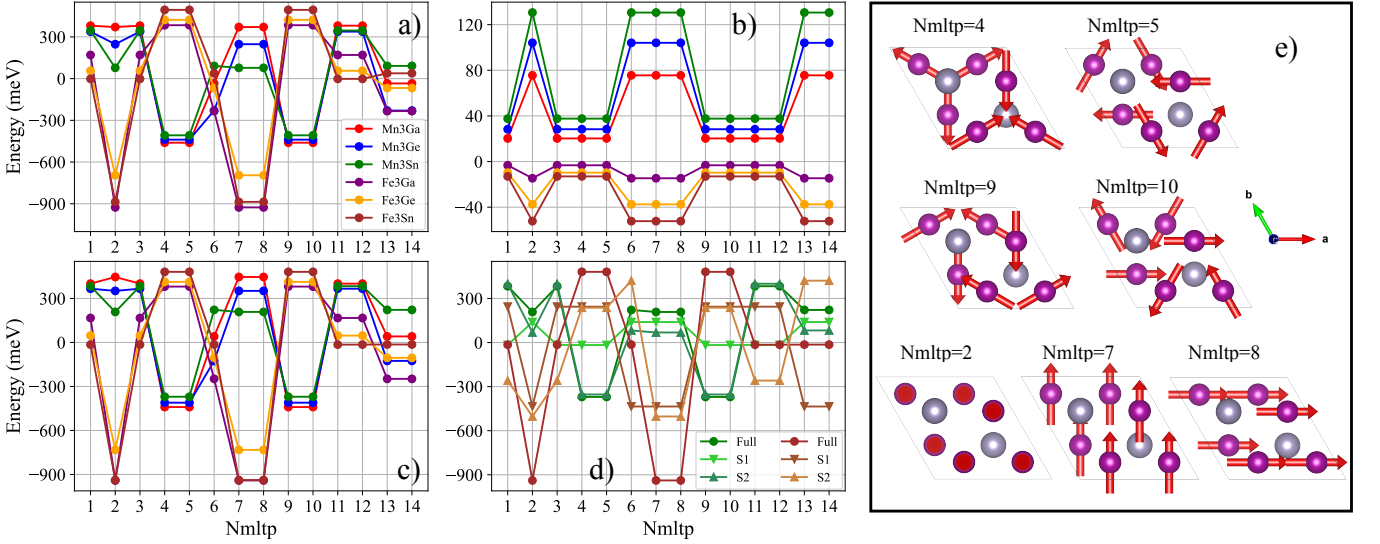


FIG. 6. a) Magnetic energy per unit cell as function of the CMP solutions considering only isotropic pair exchange interactions J_{ij} . b) Same as in (a) but considering only isotropic biquadratic exchange interactions B_{ij} . c) Same as in (a) but considering isotropic pair and biquadratic exchange interactions J_{ij} and B_{ij} . d) Magnetic energy per unit for Mn_3Sn (green curves) and Fe_3Sn (brown curves) including J_{ij} and B_{ij} . Full: Indicates energy curves that include all sublattice interactions. S1: Indicates energy curves that include only interactions within the sublattices $\{A, B, C\}$ or $\{a, b, c\}$. S2: Indicates energy curves that include only interactions from $\{A, B, C\}$ to $\{a, b, c\}$. The indexation of the sublattices follows the one given in Fig. 3. e) The minimal energy CMP solutions which features: 4 antiferromagnetic non-collinear solutions for the Mn_3X compounds and 3 collinear solutions for the Fe_3X ones.

Tm_3X	\mathcal{J}_{AA}	\mathcal{J}_{AB}	\mathcal{J}_{Aa}	\mathcal{J}_{Ab}	\mathcal{B}_{AA}	\mathcal{B}_{AB}	\mathcal{B}_{Aa}	\mathcal{B}_{Ab}
Mn_3Ga	-4.89	-11.56	35.5	-34.62	0.12	-1.12	-0.42	-5.03
Mn_3Ge	5.13	-3.32	29.88	-34.84	-0.15	-2.83	-0.37	-5.58
Mn_3Sn	-1.24	-6.41	42.25	-20.56	-0.08	-4.55	-1.03	-5.77
Fe_3Ga	1.44	47.64	7.34	25.18	-0.14	-1.25	0.05	2.51
Fe_3Ge	-5.41	34.5	-2.91	27.61	-0.01	0.02	0.09	3.07
Fe_3Sn	-3.79	37.23	-1.87	39.46	-0.15	1.02	0.14	3.34

TABLE III. Representative sublattice interaction parameters for Tm_3X compounds, including isotropic pair exchange and biquadratic exchange interactions. All coefficients are provided in units of meV.

literature [74, 77]. The common feature among all these solutions is that they present a triangular non-collinear order with a 120° relative angle within each Kagome layer, stabilized by the AFM \mathcal{J}_{AB} coupling. The moments on each sublattice are then coupled ferromagnetically to their corresponding sublattice in the second layer (e.g. A-a), stabilized by the FM \mathcal{J}_{Aa} coupling. The second group of solutions involves the Fe_3X compounds, which display three degenerate FM solutions, as depicted in Fig. 6e (Nmltp=2,7,8). The ferromagnetic order within each Kagome layer is stabilized by the large FM \mathcal{J}_{AB} , while the FM order between the layers is stabilized by the strong FM \mathcal{J}_{Ab} , despite the small negative \mathcal{J}_{Aa} , as shown in Table III.

The results obtained by including only the biquadratic terms in Eq.(16) are shown in Fig.6b. This energy exhibits more degeneracies compared to Fig. 6a, where pair interactions are considered, as it includes terms

of the form $(\mathbf{e}_n \cdot \mathbf{e}_m)^2$, which do not distinguish between FM and AFM coupled moments. Instead, it splits the states into two subgroups: one comprising collinear states (Nmltp=2,6,7,8,13,14) and the other comprising non-collinear states (Nmltp=1,3,4,5,9,10,11,12), characterized by a 120° relative angle within each Kagome layer. For Mn_3X , the biquadratic terms systematically favor a non-collinear order, whereas for Fe_3X , they favor a collinear order. This behavior is consistent with the predominantly negative (positive) \mathcal{B}_{mn} coefficients for Mn_3X (Fe_3X).

The energy of the CMP structures considering both pair and biquadratic terms is shown in Fig. 6c. The energy landscape remains similar to Fig. 6a, with modified energy barriers between collinear and non-collinear solutions due to the contributions from the biquadratic terms. The degeneracies between the CMP structures in Fig. 6a are further lifted by introducing relativistic chiral and non-chiral interactions [60, 74, 78], which will be discussed in Sec. III F. Figure 6d focuses on two compounds: Mn_3Sn (green curves) and Fe_3Sn (brown curves). Each compound has three curves: “Full”, “S1”, and “S2”. Full: indicates that the energy is calculated by including all interactions between the sublattices. S1: includes only interactions within the same sublattice group, either $\{A, B, C\}$ or $\{a, b, c\}$. These interactions stabilize non-collinear CMP solutions in Mn_3Sn and collinear ones in Fe_3Sn . S2: includes only interactions between sublattices $\{A, B, C\}$ and $\{a, b, c\}$, which are crucial for two reasons: (i) they lift the degeneracy between AFM and FM coupled mo-

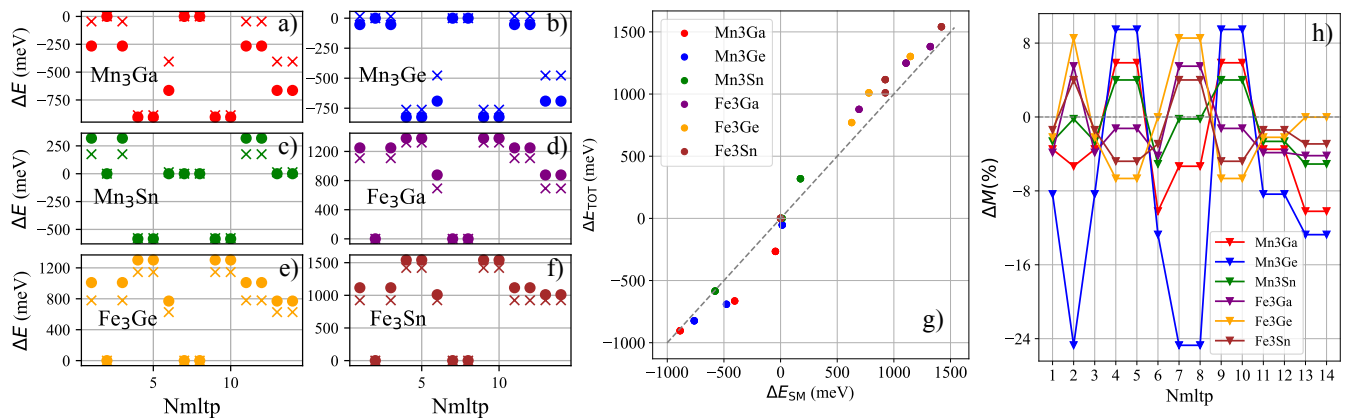


FIG. 7. a–f) Comparison of the energy differences for all Tm_3X compounds, obtained using the DLM spin model (crosses) and the total energy of constrained magnetic structures (circles), with the reference structure set to $N_{mltp}=2$ (ferromagnetic $\parallel z$ -axis). g) Deviation of the DLM spin model energies from the constrained structures; the dashed grey line indicates the $y = x$ curve. h) Deviation of the magnetic moments (ΔM) for the different constrained structures relative to the magnetic moment obtained from the charge self-consistent DLM calculations (M_{DLM}).

ments among two the Kagome layers (e.g., A–a and B–b), and (ii) in Mn_3Sn , they produce the largest energy difference between the low-energy solutions ($N_{mltp}=4,5,9,10$) and the remaining higher-energy ones.

To benchmark the energy of the CMP structures obtained from the DLM spin model (pair + biquadratic) against the total energy differences, we employ a dense $40 \times 40 \times 40$ k -mesh and self-consistently compute the total energies of the 14 CMP structures for each Tm_3X compound, accounting for a total of 84 calculations. The comparison of the energy differences ΔE , taking structure $N_{mltp}=2$ (ferromagnetic $\parallel z$ -axis) as a reference is depicted in Figs. 7a–f. To better illustrate the deviation between the spin model and the total energy calculations, we plot in Fig. 7g the energy difference ΔE_{SM} , obtained using Eq. (16), on the x -axis, and ΔE_{TOT} on the y -axis, which denotes the total energy differences obtained directly from DFT. The deviations arise from several factors, including: (i) differences between the high-temperature DLM electronic structure and the zero-temperature one obtained in the constrained calculations, (ii) the omission of multi-site higher-order magnetic interactions, (iii) the contribution of the induced magnetic moments on the X atoms, and (iv) variations in the Mn and Fe spin moment lengths among the constrained CMP structures. Despite these differences the DLM spin model successfully reproduces the global energy minima and the overall energy landscape of the CMP structures in comparison with the total energy calculations, at a significantly lower computational cost—i.e., one self-consistent DLM calculation versus 14 constrained ones for each system.

For each CMP structure, the spin moments have the same length M at every site; however, this length varies depending on the structure. Fig. 7h shows the deviation $\Delta M_{N_{mltp}} = (M_{N_{mltp}} - M_{DLM})/M_{DLM}$ of the Tm spin moments in the constrained CMP structures $M_{N_{mltp}}$

($N_{mltp}=1, \dots, 14$) relative to the DLM spin moment (M_{DLM}) given in Table I. For Mn_3X , $\Delta M_{N_{mltp}}$ exhibits a positive deviation for the lowest-energy CMP structures ($N_{mltp}=4,5,9,10$), with values of 4% for Mn_3Sn and 6% for Mn_3Ga , while the largest deviation is found for Mn_3Ge at 9.5%. These deviations become significant, reaching $\Delta M_{N_{mltp}} = -24\%$, when the non-collinear Mn_3Ge is constrained to a collinear configuration ($N_{mltp}=2,7,8$). For Fe_3X compounds, the corresponding low-energy CMP structures ($N_{mltp}=2,7,8$) exhibit a positive deviation $\Delta M_{N_{mltp}}$ of 4%–8%, whereas imposing non-collinear structures ($N_{mltp}=4,5,9,10$) systematically reduces their spin moments. These deviations underscore the challenge of selecting a reference state without prior knowledge of the lowest-energy CMP structure when constructing the spin model. This motivates our choice of the DLM reference state.

F. Relativistic interactions

Lastly, we analyze the role of the spin-orbit interaction (SOI) on lifting degeneracies of the seven lowest-energy CMP structures depicted in Fig. 6e. Considering the same computational setup as in Sec. III A, the SOI is included self-consistently [35] and rotational symmetry in spin space is broken which prevents mapping the paramagnetic DLM state onto a simple up/down binary pseudo-alloy prescription. A careful treatment requires a relativistic extension of the DLM approach [37, 79], in which averaging over multiple local-moment orientations is performed to capture the vectorial nature of thermal fluctuations [37, 53]. While we do not incorporate such advanced treatment of the spin fluctuations, we adopt a simplified approach for relativistic DLM using a pseudo-alloy with six components, corresponding to magnetic moments along the Cartesian directions $\{\pm x, \pm y, \pm z\}$, to

capture the anisotropic nature of these fluctuations [68].

On one hand, the large isotropic pair and biquadratic interactions are weakly affected by the SOI. These minor changes do not influence the energy landscape of the CMP structures shown in Fig. 6. On the other hand, the SOI generates single-ion and two-ion symmetric anisotropic interactions [74, 80] (SAI) as well as anti-symmetric Dzyaloshinskii-Moriya interactions (DMI) [74, 80], which remove the degeneracy among the identified low-energy CMP structures. Given that these structures split into two groups—non-collinear (Mn_3X) and collinear (Fe_3X)—we examine the role of the DMI in selecting the chirality for Mn_3X CMP structures and the role of the SAI in stabilizing the low-energy configuration in Fe_3X .

G. Non-collinear systems: Mn_3X

As aforementioned, we inspect the contribution of the DMI to the non-collinear magnetic order in Mn_3X , focusing on the four lowest-energy non-collinear structures in Fig. 6e. Since these structures are coplanar in the ab -plane and their cross product points along the c -axis (z -axis), only the z -component of the Dzyaloshinskii-Moriya vector D_{ij}^z contributes to the energy. D_{ij}^z is extracted via $D_{ij}^z = (\mathcal{J}_{ij}^{xy} - \mathcal{J}_{ij}^{yx})/2$ from the anisotropic pair exchange tensor components $\mathcal{J}_{ij}^{\alpha\beta}$ obtained using equation (A7), considering the averaged Green function $\mathbf{G}_{ij}(E) = \mathbf{G}_{ij}^{++z+z}(E)$. Similarly to the pair and biquadratic isotropic interactions, we introduce a sublattice model for the chiral part of the cell Hamiltonian \mathcal{H}_{ch} , which reads:

$$\mathcal{H}_{ch} = - \sum_{mn} \mathcal{D}_{mn}^z (\mathbf{e}_m \times \mathbf{e}_n)^z . \quad (17)$$

The summation m, n in the previous equations runs over all sublattices $\{A, B, C, a, b, c\}$. The sublattice DMI coefficients are given by $\mathcal{D}_{mn}^z = \sum_l D_{mn}^{z,0l}$; these are antisymmetric and obey $\mathcal{D}_{mn}^z = -\mathcal{D}_{nm}^z$, with the same sublattice contributions canceling out ($\mathcal{D}_{nn}^z = 0$). The computed DMI coefficients follow the symmetry requirements imposed by the D_{6h} point group, the details of the symmetry analysis are given in Ref. 80, which takes into account the DMI interaction within each kagome plane and the interlayer couplings. These requirements impose several restrictions on the DMI vectors, allowing for a considerable simplification of the form of Eq. (17), reducing the model to only two coefficients: \mathcal{D}_1 for interlayer and \mathcal{D}_2 for intralayer sublattice couplings. The DMI's relating inversion-symmetric sublattices vanish, leading to $\mathcal{D}_{Aa}^z = \mathcal{D}_{Bb}^z = \mathcal{D}_{Cc}^z = 0$. The intra-layer couplings are related via $\mathcal{D}_2 = \mathcal{D}_{AB}^z = -\mathcal{D}_{AC}^z = \mathcal{D}_{BC}^z$ (for $z = c/4$) and $\mathcal{D}_2 = \mathcal{D}_{ab}^z = -\mathcal{D}_{ac}^z = \mathcal{D}_{bc}^z$ (for $z = 3c/4$), while the interlayer ones are related via $\mathcal{D}_1 = \mathcal{D}_{Ab}^z = -\mathcal{D}_{Ac}^z = \mathcal{D}_{aB}^z = -\mathcal{D}_{aC}^z = \mathcal{D}_{bC}^z = \mathcal{D}_{cB}^z$.

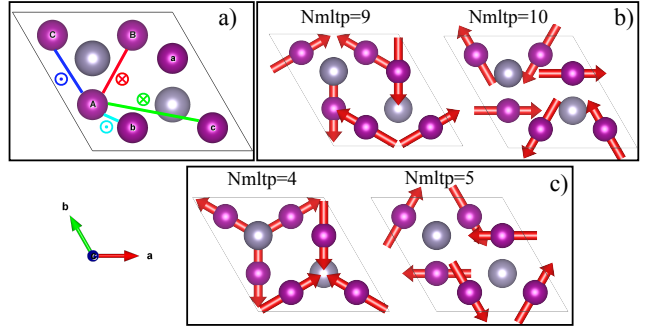


FIG. 8. a) Nonzero z -component of the sublattice Dzyaloshinskii-Moriya vector, indicated in different colors, starting from A: $\mathcal{D}_{AB} = -\mathcal{D}_{AC}$ and $\mathcal{D}_{Ab} = -\mathcal{D}_{Ac}$. b) Negative chirality (inverse triangular) structures that lower the chiral part of the Hamiltonian, \mathcal{H}_{ch} , given in Eq. (18). c) Positive chirality structures that are unfavored by \mathcal{H}_{ch} .

The chiral pair Hamiltonian simplifies as [80]:

$$\begin{aligned} \mathcal{H}_{ch} = & -2\mathcal{D}_2 [(\mathbf{e}_A \times \mathbf{e}_B)^z - (\mathbf{e}_A \times \mathbf{e}_C)^z + (\mathbf{e}_B \times \mathbf{e}_C)^z \\ & + (\mathbf{e}_a \times \mathbf{e}_b)^z - (\mathbf{e}_a \times \mathbf{e}_c)^z + (\mathbf{e}_b \times \mathbf{e}_c)^z] \\ & - 2\mathcal{D}_1 [(\mathbf{e}_A \times \mathbf{e}_b)^z - (\mathbf{e}_A \times \mathbf{e}_c)^z - (\mathbf{e}_B \times \mathbf{e}_a)^z \\ & + (\mathbf{e}_C \times \mathbf{e}_a)^z + (\mathbf{e}_B \times \mathbf{e}_c)^z - (\mathbf{e}_C \times \mathbf{e}_b)^z] . \end{aligned} \quad (18)$$

The first two lines represent the contribution of the two Kagome layers, while the last two represents the interlayer coupling. The values of \mathcal{D}_1 and \mathcal{D}_2 for the Mn_3X compounds are given in Table IV. The highest values for \mathcal{D}_1 and \mathcal{D}_2 are obtained for Mn_3Sn , followed by Mn_3Ge , and the smallest for Mn_3Ga . The chiral energy contribution $\Delta\mathcal{E}_{ch}$ is obtained from Eq. (18) using the magnetic structures given in Fig. 8b). These correspond to the inverse triangular structures discussed in Refs. 62, 78, and 80, while the structures with opposite chirality (Fig. 8c) are unstable with the opposite energy $-\Delta\mathcal{E}_{ch}$. This chiral energy contribution is two orders of magnitude smaller than the previously discussed isotropic pair and biquadratic energies, as it originates from the SOI [55]. Moreover, the interlayer and intralayer sublattice couplings are in competition, as they have opposite signs for all Mn_3X compounds. The negative chirality is fixed by \mathcal{D}_2 . The chiral energy contribution, setting \mathcal{D}_1 to zero ($\Delta\mathcal{E}_{ch}^{\text{NL}}$), is larger in magnitude compared to $\Delta\mathcal{E}_{ch}$, and the negative chirality structures are further stabilized.

The combination of single and two-ion anisotropy lifts the degeneracy between the two inverse triangular structures. A detailed discussion of the SAI on the magnetic order of Mn_3X is provided in earlier studies [74, 80]. These interactions were observed to be of weak magnitude (tens of μeV); nonetheless, they play an important role in further lifting the degeneracy among non-collinear CMP structures (Fig. 8b) and inducing net magnetic moment in the ab -plan (weak ferromagnetism) [74, 80]. Note that the analysis of weak ferromagnetism in Mn_3X requires going beyond the spin model approach presented

System	\mathcal{D}_1	\mathcal{D}_2	$\Delta\mathcal{E}_{ch}$	$\Delta\mathcal{E}_{ch}^{NL}$
Mn ₃ Ga	0.18	-0.31	-1.397	-3.266
Mn ₃ Ge	0.30	-0.41	-1.088	-4.231
Mn ₃ Sn	0.41	-0.65	-2.502	-6.724

TABLE IV. Sublattice DMI coefficients ($\mathcal{D}_1, \mathcal{D}_2$) for Mn₃X. $\Delta\mathcal{E}_{ch}$ is the chiral energy contribution for the negative chiral structures (Fig. 8b). $\Delta\mathcal{E}_{ch}^{NL}$ is the same as $\Delta\mathcal{E}_{ch}$, with \mathcal{D}_1 set to zero. All values are given in meV.

here to account for orbital polarization effects and induced moments on the X sites [78].

H. Collinear systems: Fe₃X

The magnetic anisotropy energy changes as a function of temperature [81], which is due to changes in the electronic structure as thermal spin fluctuations increase. The temperature dependence of the anisotropy energy can be extracted via the magnetic torque method [37]. It consists of single-ion and two-ion contributions, which should be distinguished when dealing with non-collinear magnetic orders [82]. Focusing on the Fe₃X which were determined to be ferromagnetic (Nmltp=2,7,8 from Fig. 6e) at zero temperature, the anisotropy energy can be expressed in terms of effective anisotropy constants \mathcal{K}_i , which are given by the sum of single-ion and two-ion contributions [37, 68]. These constants \mathcal{K}_i are determined by fitting the self-consistent total energy variations of the unit cell under global rotations of \mathbf{m}_i . The phenomenological form of the anisotropy energy $\Delta\mathcal{E}$ for the hexagonal uniaxial Fe₃X systems at hand is given by [81]:

$$\Delta\mathcal{E}(\theta, \phi) = \mathcal{K}_1 \sin^2 \theta + \mathcal{K}_2 \sin^4 \theta + \mathcal{K}_3 \sin^6 \theta + \mathcal{K}'_3 \sin^6 \theta \cos 6\phi, \quad (19)$$

where θ is the polar angle between the magnetic moment and the c -axis, and ϕ is the azimuthal angle between the moment and the a -axis. The values of $\Delta\mathcal{E}$ obtained for the Fe₃X as a function of θ are shown in Fig. 9, while the fitted values of the constants \mathcal{K}_1 and \mathcal{K}_2 are given in Table V. All the Fe₃X favor an in-plane orientation of the magnetic moments ($\theta = 90^\circ$). The largest anisotropy barrier is obtained for Fe₃Ga, intermediate for Fe₃Sn, and the lowest for Fe₃Ge. This lifts the energy degeneracy, favoring the in-plane CMP structures Nmltp=7,8 over the out-of-plane structure Nmltp=2. $\Delta\mathcal{E}$ is dominated by second-order constants with $\mathcal{K}_2 \ll \mathcal{K}_1$ and $\mathcal{K}_3 \simeq 0$. The sixth-order basal anisotropy is extremely weak, and its constant \mathcal{K}'_3 is of the order of $\simeq 1\mu\text{eV}$. Thus, in-plane CMP structures Nmltp=7,8 are quasi-degenerate. Other effects, such as small lattice distortions or doping, can contribute to lifting this degeneracy.

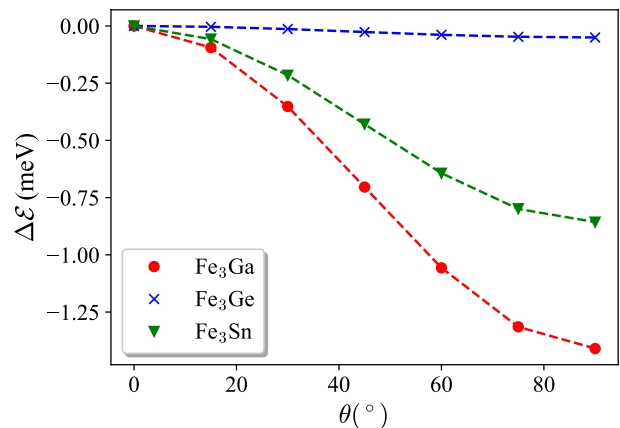


FIG. 9. Magnetic anisotropy of the Fe₃X as function of the polar angle θ . The dashed lines indicate the fits using the functional form given in Eq. (19). All the systems favor an in-plan orientation of the magnetic moments.

System	\mathcal{K}_1	\mathcal{K}_2
Fe ₃ Ga	-1.407	-0.002
Fe ₃ Ge	-0.056	0.005
Fe ₃ Sn	-0.860	0.004

TABLE V. Effective magnetic anisotropy constants \mathcal{K}_1 and \mathcal{K}_2 for the hexagonal uniaxial Fe₃X compounds. All the values are given in meV.

IV. CONCLUSIONS

We introduced a multi-scale computational approach which relies on a robust atomistic spin model parameters using the paramagnetic state as a reference, targeting both collinear and non-collinear magnetic systems. The orthogonal and complete basis of magnetic structures was systematically generated using the cluster multipole (CMP) method, bypassing the need for additional atomistic spin dynamics or Monte Carlo simulations. The Tm_3X kagome compounds provided an ideal platform to apply this approach, successfully recovering the magnetic structures reported from previous experimental and theoretical works [14, 27, 28, 62, 69, 74, 77].

The approach offers several advantages, as demonstrated for the complex Tm_3X kagome compounds, where it enables: (i) the inspection of arbitrary magnetic configurations while maintaining constant-moment solutions at minimal computational cost, (ii) the identification of commensurate or incommensurate magnetic order and a rapid estimation of the transition temperature within mean-field theory, (iii) the analysis of the role of pair and higher-order interactions in selecting low-energy CMP structures, leading to the identification of a significant biquadratic interaction contribution in Tm_3X —promoting non-collinear CMP structures in Mn₃X and collinear CMP structures in Fe₃X, (iv) the disentangling of multiple sublattice interactions, which is crucial for unit cells containing multiple atoms, as ex-

emphified by the Mn_3X compounds, where we found competing intralayer and interlayer Dzyaloshinskii–Moriya interactions (DMI), and (v) the incorporation of smaller energy-scale interactions arising from relativistic effects, including the antisymmetric DMI, which determines the chirality of the CMP structures, as well as single-ion and two-ion anisotropies, which further lift the degeneracy among the identified low-energy CMP structures.

Outlook: In this work, we focused on compounds with well-characterized magnetic structures, both theoretically and experimentally. The proposed framework provides an efficient approach for exploring material families with unknown magnetic structures by performing high-throughput computations of spin model parameters from the paramagnetic (DLM) state, combined with the CMP method, to systematically identify low-energy magnetic configurations. The low computational cost of energy evaluations at the model level enables the study of more complex cases, including magnetic order derived from linear combinations of CMP structures [19], as well as systems with large unit cells or incommensurate magnetic orders [8, 68] using a recently developed CMP extension [24]. Moreover, extending spin models beyond two-site interactions to incorporate higher-order multi-site interactions, such as isotropic four-spin interactions, allows for a more accurate description of exotic magnetic phases, including skyrmion lattices [5] and meronic phases [83].

ACKNOWLEDGMENTS

J. B. thanks Phivos Mavropoulos for fruitful discussions. J. B. was supported by the Alexander von Humboldt Foundation through the Feodor Lynen Research Fellowship for Postdocs. This work was supported by RIKEN Junior Research Associate Program. This work was supported by the RIKEN TRIP initiative (RIKEN Quantum, Advanced General Intelligence for Science Program, Many-body Electron Systems). We acknowledge the financial support by Grant-in-Aids for Scientific Research (JSPS KAKENHI) Grant Numbers JP21H04990, JP22H00290, and JP24K00581, JST-CREST No. JPMJCR23O4, JST-ASPIRE No. JPMJAP2317, JST-Mirai No. JPMJMI20A1.

Appendix A: Magnetic force theorem for ferromagnetic state

In this appendix, we recall the mapping of the magnetic interactions from the ferromagnetically ordered state, including pair [30, 32, 33] and the extension to higher order biquadratic interactions [49, 50]. The effect of spin-orbit interaction are also considered, therefore, allowing the emergence of isotropic/anisotropic pair and higher order terms in the spin Hamiltonian. The variation of the band energy is due to an infinitesimal rotation

in the magnetic exchange-correlation potential ($B^{\text{xc}}(\vec{r})$) to different orders can be easily extracted from the Lloyds formula [51, 52]:

$$\delta\mathcal{U} = -\frac{1}{\pi} \text{Im} \text{Tr}_{i\sigma} \int_{-\infty}^{E_F} dE \sum_n \frac{1}{n} (\mathcal{G}(E) \delta\mathbf{V})^n, \quad (\text{A1})$$

where \mathcal{U} is the band energy, $\mathcal{G}(E)$ is the Green function of the system, $\delta\mathbf{V}$ is the variation of potential due the infinitesimal rotation. The trace is taken over spin (σ) and sites (i). The variation of the band energy due to a two-site perturbation in the system is obtained by expanding Eq. (A1) to the second order:

$$\delta\mathcal{U}_2 = -\frac{1}{2\pi} \text{Im} \text{Tr}_{\sigma} \sum_{i \neq j} \int_{-\infty}^{E_F} dE \mathcal{G}_{ij}(E) \delta\mathbf{V}_j \mathcal{G}_{ji}(E) \delta\mathbf{V}_i. \quad (\text{A2})$$

The single particle Kohn-Sham potential at a given site i , $\mathbf{V}_i(\vec{r})$ can be splitted into a charge part $V_i^0(\vec{r})$ and a magnetic contribution $\vec{B}_i^{\text{xc}}(\vec{r})$: $V_i(\vec{r}) = V_i^0(\vec{r}) \sigma_0 + \vec{B}_i^{\text{xc}}(\vec{r}) \cdot \vec{\sigma}$, where σ_0 is 2×2 unit matrix and $\vec{\sigma} = \{\sigma_x, \sigma_y, \sigma_z\}$ is the Pauli vector. In the rigid spin approximation, the variation of the potential reads [84]:

$$\delta\mathbf{V}_i(\vec{r}) = \sum_{\alpha=x,y,z} B_i^{\text{xc}}(\vec{r}) (\delta e_i^\alpha \cdot \sigma^\alpha) \quad . \quad (\text{A3})$$

We now introduce the orbital expansion explicitly in the KKR representation of the Green function [33–35, 43] as:

$$\mathcal{G}_{ij}(\vec{r}, \vec{r}', E) = \mathbf{G}_{ii}^o(\vec{r}, \vec{r}', E) \delta_{ij} + \sum_{LL'} \mathbf{R}_{iL}(\vec{r}, E) \mathbf{G}_{ij,LL'}(E) \bar{\mathbf{R}}_{jL'}(\vec{r}', E), \quad (\text{A4})$$

$L = (l, m)$ is the angular orbital momentum expansion index, $\mathbf{G}_{ii}^o(\vec{r}, \vec{r}', E)$ is the on-site Green function which does not contribute to the magnetic interactions since $i \neq j$, $\mathbf{G}_{ij,LL'}(E)$ is the structural Green function, and $\mathbf{R}_{iL}(\vec{r}, E)$ ($\bar{\mathbf{R}}_{iL}(\vec{r}, E)$) is the right (left) regular scattering solutions. Inserting the KKR representation of the Green function (Eq. (A4)) and the explicit form $\delta\mathbf{V}_i(\vec{r})$ (Eq. (A3)) into Eq. (A2) $\delta\mathcal{U}_2$ is expressed as:

$$\delta\mathcal{U}_2 = -\frac{1}{2\pi} \text{Im} \text{Tr}_{\sigma,L} \sum_{i \neq j} \sum_{\alpha\beta} \int_{-\infty}^{E_F} dE \mathbf{G}_{ij}(E) \mathbf{B}_j^\beta(E) \mathbf{G}_{ji}(E) \mathbf{B}_i^\alpha(E) \delta e_i^\alpha \delta e_j^\beta \quad . \quad (\text{A5})$$

Note that the bold quantities in the previous equations are matrices in spin (σ) and the angular momentum L space and the trace is taken accordingly. The sum over $\{\alpha, \beta\}$ runs over the three spatial directions $\{x, y, z\}$. The matrix $\mathbf{B}_i^\alpha(E)$ as introduced as [33]:

$$\mathbf{B}_{iL_1L_2}^\alpha(E) = \int d\vec{r} \bar{\mathbf{R}}_{iL_1}(\vec{r}, E) [B_i^{\text{xc}}(\vec{r}) \sigma_\alpha] \mathbf{R}_{iL_2}(\vec{r}, E) \quad . \quad (\text{A6})$$

The analytical expression for the pair magnetic exchange interaction tensor is then obtained by mapping the internal energy variation $\delta\mathcal{U}_2$ (Eq. (A5)) onto the following pair anisotropic Heisenberg Hamiltonian: $\mathcal{H} = -\sum_{i \neq j} \sum_{\alpha\beta} \mathcal{J}_{ij}^{\alpha\beta} e_i^\alpha e_j^\beta$ leading to the expression [33, 35]:

$$\mathcal{J}_{ij}^{\alpha\beta} = \frac{1}{2\pi} \text{Im Tr}_{\sigma,L} \int_{-\infty}^{E_F} dE \quad (\text{A7})$$

$$\mathbf{G}_{ij}(E) \mathbf{B}_j^\beta(E) \mathbf{G}_{ji}(E) \mathbf{B}_i^\alpha(E) \quad .$$

The higher order interactions, in particular the biquadratic interactions are extracted from the 4th order expansion of Lloyds formula (Eq. (A1)):

$$\delta\mathcal{U}_4 = -\frac{1}{4\pi} \text{Im Tr}_\sigma \sum_{ijkl} \int_{-\infty}^{E_F} dE$$

$$\mathcal{G}_{ij}(E) \delta\mathbf{V}_j \mathcal{G}_{jk}(E) \delta\mathbf{V}_k \mathcal{G}_{kl}(E) \delta\mathbf{V}_l \mathcal{G}_{li}(E) \delta\mathbf{V}_i \quad . \quad (\text{A8})$$

Focusing the biquadratic interaction which involve only two sites, we consider the following case $k = i, l = j$ and $i \neq j$:

$$\delta\mathcal{U}_4^{\text{Biq}} = -\frac{1}{2\pi} \text{Im Tr}_\sigma \sum_{i \neq j} \int_{-\infty}^{E_F} dE$$

$$\mathcal{G}_{ij}(E) \delta\mathbf{V}_j \mathcal{G}_{ji}(E) \delta\mathbf{V}_i \mathcal{G}_{ij}(E) \delta\mathbf{V}_j \mathcal{G}_{ji}(E) \delta\mathbf{V}_i \quad . \quad (\text{A9})$$

Note that Eq. (A8) involves a double summation over $\{i, j\}$ as only two sites are considered but the interaction is of fourth order. This results in extra factor two in the above expression. Introducing the explicit form of $\delta\mathbf{V}_i$ using Eq. (A3) and the Green function's expression in the KKR basis (Eq. (A4)) results in:

$$\delta\mathcal{E}_4^{\text{Biq}} = -\frac{1}{2\pi} \text{Im Tr}_{\sigma,L} \sum_{i \neq j} \sum_{\alpha\beta\gamma\delta} \int_{-\infty}^{E_F} dE$$

$$[\mathbf{G}_{ij}(E) \mathbf{B}_j^\beta(E) \mathbf{G}_{ji}(E) \mathbf{B}_i^\alpha(E)] \quad (\text{A10})$$

$$[\mathbf{G}_{ij}(E) \mathbf{B}_j^\gamma(E) \mathbf{G}_{ji}(E) \mathbf{B}_i^\delta(E)]$$

$$\times \delta e_i^\alpha \delta e_j^\beta \delta e_i^\gamma \delta e_j^\delta$$

The mapping is then done considering an anisotropic biquadratic Hamiltonian [85]:

$$\mathcal{H}_{\text{biq}} = -\sum_{i \neq j} \sum_{\alpha\beta\gamma\delta} \mathcal{B}_{ij}^{\alpha\beta\gamma\delta} e_i^\alpha e_j^\beta e_i^\gamma e_j^\delta \quad . \quad (\text{A11})$$

A one to one identification between Eq. (A10) and Eq. (A11) provides the analytical expression of the biquadratic tensor as [49]:

$$\mathcal{B}_{ij}^{\alpha\beta\gamma\delta} = \frac{1}{2\pi} \text{Im Tr}_{\sigma,L} \int_{-\infty}^{E_F} dE \quad (\text{A12})$$

$$[\mathbf{G}_{ij}(E) \mathbf{B}_j^\beta(E) \mathbf{G}_{ji}(E) \mathbf{B}_i^\alpha(E)]$$

$$[\mathbf{G}_{ij}(E) \mathbf{B}_j^\gamma(E) \mathbf{G}_{ji}(E) \mathbf{B}_i^\delta(E)] \quad .$$

The anisotropic biquadratic tensor is of fourth rank, nonetheless, the form of \mathcal{H}_{biq} (Eq. (A11)) provides some symmetry constrains on its components. Interchanging α (β) and γ (δ) lets the Hamiltonian invariant hence one can deduce the following symmetry properties [85]: $\mathcal{B}_{ij}^{\alpha\beta\gamma\delta} = \mathcal{B}_{ij}^{\gamma\beta\alpha\delta}$, $\mathcal{B}_{ij}^{\alpha\beta\gamma\delta} = \mathcal{B}_{ij}^{\alpha\delta\gamma\beta}$, $\mathcal{B}_{ij}^{\alpha\beta\gamma\delta} = \mathcal{B}_{ij}^{\gamma\delta\alpha\beta}$.

Appendix B: Necessary isotropic and anisotropic interactions for Tm_3X compounds

The pair exchange tensor containing the $\mathcal{J}_{ij}^{\alpha\beta}$ elements can be decomposed isotropic, anti-symmetric and anisotropic symmetric parts [32, 33, 49, 55]. Considering that the magnetic moments in the ferromagnetic state point in the z -direction, the transverse part of the pair Hamiltonian accessible through the infinitesimal rotation approach can be conveniently re-expressed as:

$$\mathcal{H}^T = -\sum_{ij} J_{ij} (e_i^x e_j^x + e_i^y e_j^y) - \sum_{ij} D_{ij}^z (e_i \times e_j)^z$$

$$- \sum_{ij} S_{ij} (e_i^x e_j^x - e_i^y e_j^y) - \sum_{ij} A_{ij} (e_i^x e_j^y + e_i^y e_j^x). \quad (\text{B1})$$

The quantities introduced are the isotropic pair interaction J_{ij} , the z -component of the Dzyaloshinskii–Moriya vector (D_{ij}^z) and the two-ion anisotropy constants S_{ij} and A_{ij} . These are the central quantities of interest discussed in the main text. These constants are related to components of the pair exchange tensor via:

$$J_{ij} = \frac{\mathcal{J}_{ij}^{xx} + \mathcal{J}_{ij}^{yy}}{2}, \quad D_{ij}^z = \frac{\mathcal{J}_{ij}^{xy} - \mathcal{J}_{ij}^{yx}}{2}, \quad (\text{B2})$$

$$S_{ij} = \frac{\mathcal{J}_{ij}^{xx} - \mathcal{J}_{ij}^{yy}}{2}, \quad A_{ij} = \frac{\mathcal{J}_{ij}^{xy} + \mathcal{J}_{ij}^{yx}}{2}.$$

In the scalar relativistic limit, *i.e.* in absence of the spin-orbit interactions, the constants D_{ij}^z , S_{ij} and A_{ij} vanish [55], and the isotropic pair interaction simplifies to:

$$J_{ij} = \frac{1}{2\pi} \text{Im Tr}_{\sigma,L} \int_{-\infty}^{E_F} dE$$

$$\mathbf{G}_{ij}(E) \mathbf{B}_j^x(E) \mathbf{G}_{ji}(E) \mathbf{B}_i^x(E) \quad . \quad (\text{B3})$$

The biquadratic isotropic interactions can be extracted from the full tensor $\underline{\mathcal{B}}_{ij}$ similarly to the pair ones. Considering the transverse anisotropic symmetric part of the biquadratic Hamiltonian defined as:

$$\mathcal{H}_{\text{biq}}^T = -\sum_{i \neq j} \left[B_{ij}^{xxxx} e_i^x e_j^x e_i^x e_j^x + B_{ij}^{xxyy} e_i^x e_j^x e_i^y e_j^y \right.$$

$$\left. + B_{ij}^{yyxx} e_i^y e_j^y e_i^x e_j^x + B_{ij}^{yyyy} e_i^y e_j^y e_i^y e_j^y \right] \quad . \quad (\text{B4})$$

The latter can be re-expressed as:

$$\mathcal{H}_{\text{biq}}^T = -\sum_{i \neq j} B_{ij} \left[e_i^x e_j^x e_i^x e_j^x + e_i^x e_j^x e_i^y e_j^y \right.$$

$$\left. + e_i^y e_j^y e_i^x e_j^x + e_i^y e_j^y e_i^y e_j^y \right] + \mathcal{H}_{\text{biq}}^{\text{TA}} \quad . \quad (\text{B5})$$

$\mathcal{H}_{\text{biq}}^{\text{TA}}$ contains two-ion biquadratic anisotropic contributions of the form $(B_{ij}^{\alpha\alpha\beta\beta} - B_{ij})e_i^\alpha e_j^\alpha e_i^\beta e_j^\beta$. For periodic systems, these are generally weak, originating from a fourth-order scattering process and being second order in spin-orbit interaction. The isotropic biquadratic interactions is defined as [49]:

$$B_{ij} = \frac{B_{ij}^{xxxx} + B_{ij}^{xxyy} + B_{ij}^{yyxx} + B_{ij}^{yyyy}}{4} . \quad (\text{B6})$$

Once more, in the scalar relativistic limit the anisotropic contributions vanish and $\mathcal{H}_{\text{biq}}^{\text{TA}} = 0$. The B_{ij} constant is then simply given by:

$$B_{ij} = \frac{1}{2\pi} \text{Im Tr}_{\sigma,L} \int_{-\infty}^{E_F} dE \begin{bmatrix} \mathbf{G}_{ij}(E) \mathbf{B}_j^x(E) \mathbf{G}_{ji}(E) \mathbf{B}_i^x(E) \\ \mathbf{G}_{ij}(E) \mathbf{B}_j^x(E) \mathbf{G}_{ji}(E) \mathbf{B}_i^x(E) \end{bmatrix} . \quad (\text{B7})$$

Appendix C: Complete CMP generated structures

The complete set of cluster multipole structures generated for Tm_3X (space group $P6_3/mmc$) up to $l = 3$ is depicted in Fig. 10a. These structures are labeled with an integer index (Nmltp) and correspond to the respective magnetic ($\mathcal{M}_{l\gamma}$) and toroidal ($\mathcal{T}_{l\gamma}$) multipoles introduced in Eq. (1) of the main text. The simplest solutions are the dipole structures $\mathcal{M}_{1\gamma}$, which represent three collinear magnetic structures with moments \mathbf{m}_i oriented along the (x, y, z) spatial directions (Nmltp= 2, 7, 8). These structures account for spin-orbit anisotropy, as the CMP approach is based on the magnetic space group [22]. Fig. 10b shows toroidal moment structures involving *large* longitudinal variations in the magnitude of \mathbf{m}_i . These structures involving drastic changes in the magnetic moment lengths are higher in energy and not considered in the evaluation of CMP energies in Sec. III E. Our model analysis focuses on the low-energy configurations that involve directional changes of the magnetic moments while keeping their length fixed (transverse variations), as the Tm atoms have local moments, for which the DLM approach provides a good description.

-
- [1] W. Heisenberg, Zur theorie des ferromagnetismus, *Zeitschrift für Physik* **49**, 619 (1928).
- [2] L. Néel, Propriétés magnétiques des ferrites; et antiferromagnétisme, *Annales de Physique (Paris)* **5**, 232 (1948).
- [3] L. Šmejkal, J. Sinova, and T. Jungwirth, Emerging research landscape of altermagnetism, *Phys. Rev. X* **12**, 040501 (2022).
- [4] I. Hughes, M. Däne, A. Ernst, W. Hergert, M. Lüders, J. Poulter, J. B. Staunton, A. Svane, Z. Szotek, and W. Temmerman, Lanthanide contraction and magnetism in the heavy rare earth elements, *Nature* **446**, 650 (2007).
- [5] S. Heinze, K. Von Bergmann, M. Menzel, J. Brede, A. Kubetzka, R. Wiesendanger, G. Bihlmayer, and S. Blügel, Spontaneous atomic-scale magnetic skyrmion lattice in two dimensions, *nature physics* **7**, 713 (2011).
- [6] S. Grytsiuk, J.-P. Hanke, M. Hoffmann, J. Bouaziz, O. Gomonay, G. Bihlmayer, S. Lounis, Y. Mokrousov, and S. Blügel, Topological-chiral magnetic interactions driven by emergent orbital magnetism, *Nature communications* **11**, 511 (2020).
- [7] S. Nakatsuji and R. Arita, Topological magnets: functions based on berry phase and multipoles, *Annual Review of Condensed Matter Physics* **13**, 119 (2022).
- [8] J. Bouaziz, E. Mendive-Tapia, S. Blügel, and J. B. Staunton, Fermi-surface origin of skyrmion lattices in centrosymmetric rare-earth intermetallics, *Phys. Rev. Lett.* **128**, 157206 (2022).
- [9] J. Bouaziz, G. Bihlmayer, C. E. Patrick, J. B. Staunton, and S. Blügel, Origin of incommensurate magnetic order in the $R\text{AlSi}$ magnetic weyl semimetals ($R = \text{Pr, Nd, Sm}$), *Phys. Rev. B* **109**, L201108 (2024).
- [10] S. Hayami and Y. Motome, Topological spin crystals by itinerant frustration, *Journal of Physics: Condensed Matter* **33**, 443001 (2021).
- [11] N. Nagaosa and Y. Tokura, Topological properties and dynamics of magnetic skyrmions, *Nature nanotechnology* **8**, 899 (2013).
- [12] J.-R. Soh, I. Sánchez-Ramírez, X. Yang, J. Sun, I. Zivkovic, J. A. Rodríguez-Velamazán, O. Fabelo, A. Stunault, A. Bombardi, C. Balz, et al., Weyl metallic state induced by helical magnetic order, *npj Quantum Materials* **9**, 7 (2024).
- [13] J. Kübler and C. Felser, Non-collinear antiferromagnets and the anomalous hall effect, *Europhysics Letters* **108**, 67001 (2014).
- [14] S. Nakatsuji, N. Kiyohara, and T. Higo, Large anomalous hall effect in a non-collinear antiferromagnet at room temperature, *Nature* **527**, 212 (2015).
- [15] V. Baltz, A. Manchon, M. Tsoi, T. Moriyama, T. Ono, and Y. Tserkovnyak, Antiferromagnetic spintronics, *Reviews of Modern Physics* **90**, 015005 (2018).
- [16] V. Bonbien, F. Zhuo, A. Salimath, O. Ly, A. About, and A. Manchon, Topological aspects of antiferromagnets, *Journal of Physics D: Applied Physics* **55**, 103002 (2021).
- [17] S. Mühlbauer, D. Honecker, E. A. Périgo, F. Bergner, S. Disch, A. Heinemann, S. Erokhin, D. Berkov, C. Leighton, M. R. Eskildsen, and A. Michels, Magnetic small-angle neutron scattering, *Rev. Mod. Phys.* **91**, 015004 (2019).
- [18] Y. Xu, L. Elcoro, Z.-D. Song, B. J. Wieder, M. Vergniory, N. Regnault, Y. Chen, C. Felser, and B. A. Bernevig, High-throughput calculations of magnetic topological materials, *Nature* **586**, 702 (2020).
- [19] M.-T. Huebsch, T. Nomoto, M.-T. Suzuki, and R. Arita, Benchmark for ab initio prediction of magnetic struc-

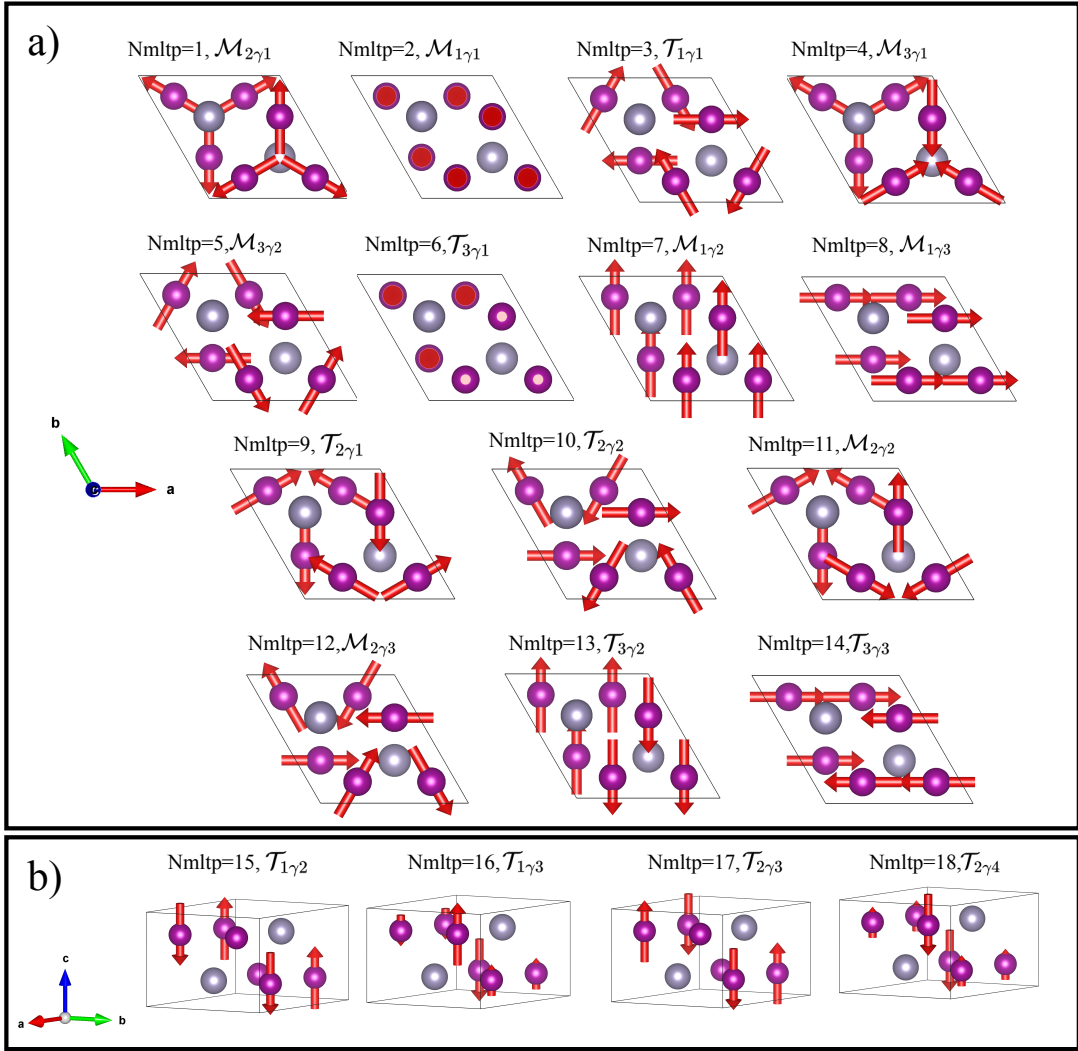


FIG. 10. Generated CMP structures up to $l = 3$. (a) Magnetic ($\mathcal{M}_{l\gamma}$) and toroidal ($\mathcal{T}_{l\gamma}$) multipole structures, including collinear and non-collinear ones, that conserve the length of the magnetic moment \mathbf{m}_i are considered in this energy evaluation in Sec. III E. (b) High-energy toroidal multipole structures involving large variations of the length of \mathbf{m}_i .

- tures based on cluster-multipole theory, *Phys. Rev. X* **11**, 011031 (2021).
- [20] T. Nomoto, S. Minami, Y. Yanagi, M.-T. Suzuki, T. Koretsune, and R. Arita, High-throughput calculations of antiferromagnets hosting anomalous transport phenomena, *Phys. Rev. B* **109**, 094435 (2024).
- [21] M.-T. Suzuki, T. Koretsune, M. Ochi, and R. Arita, Cluster multipole theory for anomalous hall effect in antiferromagnets, *Phys. Rev. B* **95**, 094406 (2017).
- [22] M.-T. Suzuki, T. Nomoto, R. Arita, Y. Yanagi, S. Hayami, and H. Kusunose, Multipole expansion for magnetic structures: A generation scheme for a symmetry-adapted orthonormal basis set in the crystallographic point group, *Phys. Rev. B* **99**, 174407 (2019).
- [23] M.-T. Suzuki, H. Ikeda, and P. M. Oppeneer, First-principles theory of magnetic multipoles in condensed matter systems, *Journal of the Physical Society of Japan* **87**, 041008 (2018).
- [24] Y. Yanagi, H. Kusunose, T. Nomoto, R. Arita, and M.-T. Suzuki, Generation of modulated magnetic structures based on cluster multipole expansion: Application to α -Mn and CoM_3S_6 , *Phys. Rev. B* **107**, 014407 (2023).
- [25] K. Sato, L. Bergqvist, J. Kudrnovský, P. H. Dederichs, O. Eriksson, I. Turek, B. Sanyal, G. Bouzerar, H. Katayama-Yoshida, V. A. Dinh, T. Fukushima, H. Kizaki, and R. Zeller, First-principles theory of dilute magnetic semiconductors, *Rev. Mod. Phys.* **82**, 1633 (2010).
- [26] E. Krén and G. Kádár, Neutron diffraction study of Mn_3Ga , *Solid State Communications* **8**, 1653 (1970).
- [27] B. C. Sales, B. Sagarov, M. A. McGuire, D. J. Singh, and D. S. Parker, Ferromagnetism of Fe_3Sn and alloys, *Scientific reports* **4**, 7024 (2014).
- [28] Z. Li, Y. Wang, Z. Xia, Q. Zhang, Z. Li, E. Liu, and Z. Liu, Anomalous hall effect dominated by intrinsic mechanism in Fe_3Ge with hexagonal DO19 kagome lattice and cubic DO3 structure, *Applied Physics Letters*

- 122**, 032401 (2023).
- [29] T. Oguchi, K. Terakura, and N. Hamada, Magnetism of iron above the curie temperature, *Journal of Physics F: Metal Physics* **13**, 145 (1983).
- [30] A. I. Liechtenstein, M. I. Katsnelson, and V. A. Gubanov, Exchange interactions and spin-wave stiffness in ferromagnetic metals, *Journal of Physics F: Metal Physics* **14**, L125 (1984).
- [31] I. Turek, J. Kudrnovský, V. Drchal, and P. Bruno, Exchange interactions, spin waves, and transition temperatures in itinerant magnets, *Philosophical Magazine* **86**, 1713 (2006).
- [32] L. Udvardi, L. Szunyogh, K. Palotás, and P. Weinberger, First-principles relativistic study of spin waves in thin magnetic films, *Phys. Rev. B* **68**, 104436 (2003).
- [33] H. Ebert and S. Mankovsky, Anisotropic exchange coupling in diluted magnetic semiconductors: Ab initio spin-density functional theory, *Phys. Rev. B* **79**, 045209 (2009).
- [34] N. Papanikolaou, R. Zeller, and P. H. Dederichs, Conceptual improvements of the kkr method, *Journal of Physics: Condensed Matter* **14**, 2799 (2002).
- [35] D. S. G. Bauer, Development of a relativistic full-potential first-principles multiple scattering green function method applied to complex magnetic textures of nanostructures at surfaces, PhD Dissertation, RWTH Aachen University (2014).
- [36] B. L. Gyorffy, A. J. Pindor, J. Staunton, G. M. Stocks, and H. Winter, A first-principles theory of ferromagnetic phase transitions in metals, *Journal of Physics F: Metal Physics* **15**, 1337 (1985).
- [37] J. B. Staunton, L. Szunyogh, A. Buruzs, B. L. Gyorffy, S. Ostanin, and L. Udvardi, Temperature dependence of magnetic anisotropy: An ab initio approach, *Phys. Rev. B* **74**, 144411 (2006).
- [38] P. Soven, Coherent-potential model of substitutional disordered alloys, *Phys. Rev.* **156**, 809 (1967).
- [39] J. D. Jackson, *Classical Electrodynamics*, 2nd ed. (Wiley, New York, 1975).
- [40] H. Kusunose, Description of multipole in f-electron systems, *Journal of the Physical Society of Japan* **77**, 064710 (2008).
- [41] S. V. Gallego, J. M. Perez-Mato, L. Elcoro, E. S. Tasci, R. M. Hanson, K. Momma, M. I. Aroyo, and G. Madariaga, Magndata: towards a database of magnetic structures. i. the commensurate case, *Journal of Applied Crystallography* **49**, 1750 (2016).
- [42] J. B. Staunton and B. L. Gyorffy, Onsager cavity fields in itinerant-electron paramagnets, *Phys. Rev. Lett.* **69**, 371 (1992).
- [43] H. Ebert, D. Ködderitzsch, and J. Minár, Calculating condensed matter properties using the kkr-green's function method—recent developments and applications, *Reports on Progress in Physics* **74**, 096501 (2011).
- [44] J. Staunton, B. Gyorffy, G. Stocks, and J. Wadsworth, The static, paramagnetic, spin susceptibility of metals at finite temperatures, *Journal of Physics F: Metal Physics* **16**, 1761 (1986).
- [45] H. Akai and P. Dederichs, Local moment disorder in ferromagnetic alloys, *Physical Review B* **47**, 8739 (1993).
- [46] H. Akai, Ferromagnetism and its stability in the diluted magnetic semiconductor (in, mn)as, *Phys. Rev. Lett.* **81**, 3002 (1998).
- [47] P. Bruno, J. Kudrnovský, V. Drchal, and I. Turek, Interlayer exchange coupling: The effect of substitutional disorder, *Phys. Rev. Lett.* **76**, 4254 (1996).
- [48] J. Staunton, B. L. Gyorffy, J. Poulter, and P. Strange, The relativistic rky interaction, uniaxial and unidirectional magnetic anisotropies and spin glasses, *Journal of Physics: Condensed Matter* **1**, 5157 (1989).
- [49] S. Mankovsky, S. Polesya, and H. Ebert, Extension of the standard heisenberg hamiltonian to multispin exchange interactions, *Phys. Rev. B* **101**, 174401 (2020).
- [50] S. Lounis, Multiple-scattering approach for multi-spin chiral magnetic interactions: application to the one- and two-dimensional rashba electron gas, *New Journal of Physics* **22**, 103003 (2020).
- [51] P. Lloyd and P. Smith, Multiple scattering theory in condensed materials, *Advances in Physics* **21**, 69 (1972).
- [52] B. Drittler, M. Weinert, R. Zeller, and P. Dederichs, First-principles calculation of impurity-solution energies in cu and ni, *Physical Review B* **39**, 930 (1989).
- [53] L. Szunyogh, L. Udvardi, J. Jackson, U. Nowak, and R. Chantrell, Atomistic spin model based on a spin-cluster expansion technique: Application to the irmn₃/co interface, *Phys. Rev. B* **83**, 024401 (2011).
- [54] T. Hatanaka, J. Bouaziz, T. Nomoto, and R. Arita, Calculation of the biquadratic spin interactions based on the spin cluster expansion for ab initio tight-binding models, arXiv:2405.04369 (2024).
- [55] J. Bouaziz, M. dos Santos Dias, A. Ziane, M. Benakki, S. Blügel, and S. Lounis, Chiral magnetism of magnetic adatoms generated by rashba electrons, *New Journal of Physics* **19**, 023010 (2017).
- [56] I. Dzyaloshinsky, Theory of helicoidal structures in antiferromagnets, *Journal of Experimental and Theoretical Physics (U.S.S.R.)* **74**, 992 (1964).
- [57] T. Moriya, Anisotropic superexchange interaction and weak ferromagnetism, *Physical Review* **120**, 91 (1960).
- [58] P. Rüßmann, D. Antognini Silva, G. Géranton, D. S. G. Bauer, P. Baumeister, P. F. Bornemann, J. Bouaziz, S. Brinker, J. Chico, P. H. Dederichs, B. H. Drittler, F. Dos Santos, M. dos Santos Dias, N. Essing, I. Klepetsanis, A. Kosma, N. H. Long, S. Lounis, P. Mavropoulos, E. Mendive Tapia, C. Oran, N. Papanikolaou, E. Rabel, B. Schweffinghaus, N. Stefanou, A. R. Thiess, R. Zeller, B. Zimmermann, and S. Blügel, *JuDFTteam/JuKKR: v3.6; v3.6* (2022).
- [59] A. J. Pindor, J. Staunton, G. M. Stocks, and H. Winter, Disordered local moment state of magnetic transition metals: a self-consistent kkr cpa calculation, *Journal of Physics F: Metal Physics* **13**, 979 (1983).
- [60] P. Park, J. Oh, K. Uhlířová, J. Jackson, A. Deák, L. Szunyogh, K. H. Lee, H. Cho, H.-L. Kim, H. C. Walker, et al., Magnetic excitations in non-collinear antiferromagnetic weyl semimetal Mn₃Sn, *npj Quantum Materials* **3**, 63 (2018).
- [61] G. Kádár and E. Krén, Neutron diffraction study of Mn₃Ge, *Int. J. Magn* **1**, 143 (1971).
- [62] J.-R. Soh, F. de Juan, N. Qureshi, H. Jacobsen, H.-Y. Wang, Y.-F. Guo, and A. T. Boothroyd, Ground-state magnetic structure of Mn₃Ge, *Phys. Rev. B* **101**, 140411 (2020).
- [63] J. Cable, N. Wakabayashi, and P. Radhakrishna, A neutron study of the magnetic structure of Mn₃Sn, *Solid state communications* **88**, 161 (1993).

- [64] J.-J. Couderg, J. Bras, and M. Fagot, Etude de la structure ordonnee de l'alliage Fe_3Ga , Comptes Rendus des Seances de l'Academie des Sciences, Serie B: Sciences Physiques **272**, 781 (1971).
- [65] Z. Li, M. Liu, D. Wang, E. Liu, and Z. Liu, Tuning the anomalous hall effect of the high curie temperature nodal-line metal Fe_3Ga via mn doping and associated band topology, *Phys. Rev. B* **110**, 104407 (2024).
- [66] R. Andrusyak and B. Kotur, Phase equilibriums in the Sc-Mn-Ge and Sc-Fe-Ge systems at 870 K, Russian Metallurgy (English Translation) **1991**, 204 (1991), (17 structures).
- [67] K. Buschow, P. van Engen, and R. Jongebreur, Magneto-optical properties of metallic ferromagnetic materials, Journal of Magnetism and Magnetic Materials **38**, 1 (1983), (190 structures).
- [68] J. Bouaziz, C. E. Patrick, and J. B. Staunton, Crucial role of Fe in determining the hard magnetic properties of $\text{Nd}_2\text{Fe}_{14}\text{B}$, *Phys. Rev. B* **107**, L020401 (2023).
- [69] E. Mendive-Tapia and J. B. Staunton, Ab initio theory of the gibbs free energy and a hierarchy of local moment correlation functions in itinerant electron systems: The magnetism of the Mn_3A materials class, *Phys. Rev. B* **99**, 144424 (2019).
- [70] T. Duan, W. Ren, W. Liu, S. Li, W. Liu, and Z. Zhang, Magnetic anisotropy of single-crystalline Mn_3Sn in triangular and helix-phase states, Applied Physics Letters **107** (2015).
- [71] Y. Chen, J. Gaudet, G. G. Marcus, T. Nomoto, T. Chen, T. Tomita, M. Ikhlas, H. S. Suzuki, Y. Zhao, W. C. Chen, J. Stremper, R. Arita, S. Nakatsuji, and C. Broholm, Intertwined charge and spin density waves in a topological kagome material, *Phys. Rev. Res.* **6**, L032016 (2024).
- [72] G. Zimmer and E. Krén, Investigation of the magnetic phase transformation in Mn_3Sn , in *AIP Conference Proceedings*, Vol. 5 (American Institute of Physics, 1972) pp. 513–516.
- [73] A. Akbari, P. Thalmeier, and I. Eremin, Evolution of the multiband ruderman–kittel–kasuya–yosida interaction: application to iron pnictides and chalcogenides, New Journal of Physics **15**, 033034 (2013).
- [74] B. Nyári, A. Deák, and L. Szunyogh, Weak ferromagnetism in hexagonal Mn_3Z alloys ($Z = \text{Sn, Ge, Ga}$), *Phys. Rev. B* **100**, 144412 (2019).
- [75] E. Simon, A. Donges, L. Szunyogh, and U. Nowak, Noncollinear antiferromagnetic states in ru-based heusler compounds induced by biquadratic coupling, *Phys. Rev. Mater.* **4**, 084408 (2020).
- [76] M. dos Santos Dias, S. Brinker, A. Lászlóffy, B. Nyári, S. Blügel, L. Szunyogh, and S. Lounis, Proper and improper chiral magnetic interactions, *Phys. Rev. B* **103**, L140408 (2021).
- [77] J. Sticht, K. Höck, and J. Kübler, Non-collinear itinerant magnetism: the case of Mn_3Sn , Journal of Physics: Condensed Matter **1**, 8155 (1989).
- [78] L. M. Sandratskii and J. Kübler, Role of orbital polarization in weak ferromagnetism, *Phys. Rev. Lett.* **76**, 4963 (1996).
- [79] J. B. Staunton, S. Ostanin, S. S. A. Razee, B. L. Gyorffy, L. Szunyogh, B. Ginatempo, and E. Bruno, Temperature dependent magnetic anisotropy in metallic magnets from an ab initio electronic structure theory: 11_0 -ordered fept, *Phys. Rev. Lett.* **93**, 257204 (2004).
- [80] A. Zelenskiy, T. L. Monchesky, M. L. Plumer, and B. W. Southern, Anisotropic magnetic interactions in hexagonal ab -stacked kagome lattice structures: Application to Mn_3X ($X=\text{Ge,Sn,Ga}$) compounds, *Phys. Rev. B* **103**, 144401 (2021).
- [81] R. Skomski, *Simple models of magnetism* (Oxford university press, 2008).
- [82] D. Amoroso, P. Barone, and S. Picozzi, Spontaneous skyrmionic lattice from anisotropic symmetric exchange in a Ni-halide monolayer, Nature communications **11**, 5784 (2020).
- [83] N. D. Khanh, T. Nakajima, S. Hayami, S. Gao, Y. Yamasaki, H. Sagayama, H. Nakao, R. Takagi, Y. Motome, Y. Tokura, *et al.*, Zoology of multiple-q spin textures in a centrosymmetric tetragonal magnet with itinerant electrons, Advanced Science **9**, 2105452 (2022).
- [84] P. Phariseau and B. Gyorffy, *Electrons in disordered metals and at metallic surfaces*, Vol. 42 (Springer Science & Business Media, 2012).
- [85] S. Brinker, M. d. S. Dias, and S. Lounis, The chiral biquadratic pair interaction, New journal of physics **21**, 083015 (2019).